TECHNISCHE
UNIVERSITÄT
WIEN
Vienna University of Technology

DIPLOMARBEIT

Finite Temperature Modelling of Fe-Ni Invar-Alloys based on ab-initio Energy Calculations

ausgeführt am
Institut für Angewandte Physik
der Technischen Universität Wien

unter der Anleitung von
Univ.Prof. Dipl.-Ing. Dr.techn. Peter Mohn

durch

Roland Bliem
Siebenbrunnengasse 8/4
1050 Wien

Wien, 27. November 2012 _____

Abstract

In most models the Invar anomaly is explained on the basis of magnetic effects only, neglecting structural contributions. Since the Fe-Ni Invar concentration range overlaps with the range where the martensitic transformation occurs, the present work examines the combination of magnetic and structural effects in static ab-initio calculations of the Invar model systems Fe_3Ni and Fe_5Ni_3 at various different volumes and tetragonal deformations. Based on the results, finite temperature effects of the structural part described by the cell volume and the tetragonal deformation are studied. The temperature is introduced to the system in the form of local fluctuations of the volume and c/a-ratio, which are described within a Ginzburg-Landau model.

The static ab-initio calculations and relaxations show that the ground state for Fe_3Ni is the bcc-like structure ($L1_2$ structure tetragonally deformed to $c/a = 1/\sqrt{2}$) whereas in Fe_5Ni_3 it is the fcc-like structure ($L1_2$). In both cases the energy barrier of the martensitic transformation is approximately one order of magnitude higher in the non-magnetic case.

In order to make the range of compositions between the model systems available, analytical expressions for the energy as a function of volume and tetragonal deformation are determined, making an interpolation between the two compositions possible.

In the finite temperature model the martensitic transformation is analysed and the temperature dependence of the thermal expansion coefficient, the bulk modulus, and the elastic constant C' are determined. A structural transformation is only found in systems, in which the bcc-like state is the ground state. For Fe_3Ni, the fcc-like state exhibits a small negative thermal expansion coefficient, which could be a necessary property for the Invar effect in these alloys.

Kurzfassung

In den meisten Modellen wird die Invar-Anomalie ausschließlich durch magnetische Effekte erklärt, wobei strukturelle Beiträge vernachlässigt werden. Da aber der Invar Effekt in Fe-Ni Legierungen in einem Konzentrationsbereich auftritt, der sich mit dem der martensitischen Transformation überschneidet, wird in der vorliegenden Diplomarbeit das Zusammenwirken magnetischer und struktureller Effekte in statischen ab-initio Rechnungen der Invar Modellsysteme Fe_3Ni und Fe_5Ni_3 bei verschiedenen Volumina und tetragonalen Verzerrungen untersucht. Aufbauend auf den Resultaten dieser Rechnungen werden strukturelle Effekte, beschrieben durch das Volumen und die tetragonale Verzerrung, bei endlicher Temperatur analysiert. Die Temperatur wird in Form von lokalen Fluktuationen der Variablen, die im Rahmen eines Ginzburg-Landau Modells beschrieben werden, in das System eingekoppelt.

Die statischen ab-initio Rechnungen und zusätzlich durchgeführte Relaxationen des Gitters zeigen, dass die bcc-artige Struktur (eine tetragonal zu $c/a = 1/\sqrt{2}$ verzerrte $L1_2$-Struktur) den Grundzustand von Fe_3Ni darstellt. Für Fe_5Ni_3 hingegen ist der Grundzustand durch die fcc-artige $L1_2$-Struktur gegeben. In beiden Systemen ist die Energiebarriere der martensitischen Transformation im nichtmagnetischen Fall um circa eine Größenordnung höher.

Um den Konzentrationsbereich zwischen den Modellsystemen für weiterführende Rechnungen zugänglich zu machen, werden analytische Ausdrücke für die Energie der Modellsysteme als Funktion des Volumens und des c/a-Verhältnisses bestimmt. Dadurch ist es möglich, beliebige Konzentrationen im Zwischenbereich durch Interpolation zu erreichen.

In den Berechnungen mit endlicher Temperatur wird der martensitische Übergang analysiert und die Temperaturabhängigkeit des thermischen Ausdehnungskoeffizienten, des Bulkmoduls und der elastischen Konstante C' bestimmt. Ein struktureller Übergang tritt ausschließlich in Systemen auf, in denen der Grundzustand bcc-artig ist. In Fe_3Ni zeigt der fcc-artige Zustand einen kleinen negativen thermischen Ausdehnungskoeffizienten, was möglicherweise eine notwendige Eigenschaft für das Auftreten von Invar-Verhalten in diesen Legierungen ist.

Contents

1 Motivation

In 1897, Charles Édouard Guillaume discovered that the alloy $Fe_{65}Ni_{35}$ exhibits almost zero thermal expansion over a wide temperature range [1]. Since then, many theories have been developed to explain this behaviour called the Invar effect, a selection of which is presented in section 2.2.1. Most of these theories explain the Invar behaviour on the basis of magnetic effects, neglecting possible structural contributions.
In private communication Dr Xiaobing Ren working at Xi'an Jiaotong University, China, explained the Invar effect on the basis of the formation of strain glass regions in the material, which are similar to a tweed-like structural intermixture of an fcc-like and a bcc-like phase and compensate for the thermal expansion of the lattice. Since this approach is not directly based on the magnetic effects, which are the basis of most of the theories of the Invar effect, it starts from an absolutely different perspective, which could improve the understanding of the effect. However, since completely neglecting magnetism in a ferromagnetic material probably leads to an incomplete description, the significance of magnetism to the structural effects in the Invar system has to be included. Hence the aim of the present work is to find a connection between the existing theories and structural effects by investigating the importance of magnetism in structural transitions and by simulating the temperature dependence of the system based only on structural variables. The findings suggest that structural transitions in Fe-Ni Invar are highly improbable without magnetic effects but also that structural effects contribute an important part to the behaviour of the system.

2 Introduction

2.1 Theoretical Background

The aim of electronic structure calculations is to gain information on properties of a complex quantum mechanical system starting from basic knowledge of the different contributions to its total energy. All the information contained in a system is described by its Schrödinger equation and boundary conditions. The solution of the Schrödinger equation gives the system's wave functions, from which all essential properties of the system can be deduced. For many-body calculations, which are necessary in solid state physics, a direct solution of the Schrödinger equation is not possible. Thus different approaches are required.
Still, the Schrödinger equation remains the starting point of theoretical considerations in electronic structure calculations. A very common approximation in solid state calculations is the Born-Oppenheimer approximation, which assumes that the ionic and the electronic energy of the system can be separated. The respective Schrödinger equation for an N electron system interacting with the potential of an ionic lattice is given by equation 2.1.

$$\begin{aligned} \widehat{H} \quad & \Psi(\mathbf{x_1}, ..., \mathbf{x_N}) = E\Psi(\mathbf{x_1}, ..., \mathbf{x_N}) \\ \widehat{H} \quad & = \sum_{i=1}^{N}(-\tfrac{1}{2}\nabla_i^2) + \sum_{i=1}^{N} v_{ne}(\mathbf{r}_i) + \sum_{i<j}^{N} \tfrac{1}{r_{ij}} \end{aligned} \tag{2.1}$$

The first term represents the kinetic energy, v_{ne} the interaction with the lattice potential and the third term the Coulomb interaction of the electrons. $\widehat{H}$ is the Hamiltonian of the electronic system; the purely ionic part of the energy is not included in this

representation. It should be noted that the first and the third term of $\widehat{H}$ are universal, which means that they do not depend on the lattice potential but only on the total number of electrons N.
In order to calculate the total ground state energy, the lattice contribution (repulsion of the nuclei) has to be added explicitly to the eigenvalue of the electronic ground state.
To achieve a physically meaningful description of an N-electron system, the wave function must fulfil certain conditions (see equation 2.2).

$$\begin{aligned} \Psi(\mathbf{x}_1, ..., \mathbf{x}_i, \mathbf{x}_j ...) &= -\Psi(\mathbf{x}_1, ..., \mathbf{x}_j, \mathbf{x}_i ...) \qquad \text{Pauli Principle} \\ \langle \Psi_i \mid \Psi_j \rangle &= \delta_{i,j} \qquad\qquad\qquad\qquad \text{Orthonormalization} \end{aligned} \tag{2.2}$$

Since the energy of the system is the expectation value of $\widehat{H}$, it can be expressed as a functional of Ψ. It can be shown that minimization of this functional with respect to Ψ results in the ground state energy E_0 and its wave function Ψ_0. Any meaningful approximative wave function different from the exact ground state leads to a higher energy of the system.
Since $\widehat{H}$ is uniquely described by the number of electrons N and the lattice potential v_{ne}, these two properties combined with appropriate boundary conditions also determine the ground state energy E_0, its wave function Ψ_0 and its electron density $\rho(\mathbf{r})$. Hence, the ground state energy can not only be written as a functional of Ψ but also as a functional of N and v_{ne}.

2.1.1 Density Functional Theory

A very successful approach to describe a many-particle system is *Density Functional Theory* (DFT), which is based on the previously mentioned properties of many-body Hamiltonians. DFT circumvents the necessity to solve the many-particle Schrödinger equation by mapping all the system's properties to the electron density. The starting point for *Density Functional Theory* was in 1964, when Hohenberg and Kohn [2] proved that the ground state energy is a unique functional of the electron density, meaning that $\rho(\mathbf{r})$ determines $\widehat{H}$ and therefore Ψ. This is known as the first Hohenberg-Kohn theorem. The second Hohenberg-Kohn theorem states that one can apply the variational principle

to minimize the energy. The variation of the density leads to equation 2.3, with the universal Hohenberg-Kohn functional F_{HK}, consisting of the kinetic energy and the electron-electron interaction.

$$\frac{\delta E[\rho]}{\delta \rho(\mathbf{r})} = v(\mathbf{r}) + \frac{\delta F_{HK}[\rho]}{\delta \rho(\mathbf{r})} \tag{2.3}$$

The large drawback of equation 2.3 is that its solution requires an explicit form of the Hohenberg-Kohn functional of the full electronic system.
In 1965 Kohn and Sham [3] reformulated Density Functional Theory by mapping it to a non-interacting system, meaning that the total electronic energy is decomposed as in equation 2.4.

$$E[\rho] = T_S[\rho] + \frac{1}{2}\int\int \frac{n(\mathbf{r})n(\mathbf{r}')}{|\mathbf{r}-\mathbf{r}'|} d\mathbf{r}d\mathbf{r}' + \int v(\mathbf{r})n(\mathbf{r})d\mathbf{r} + E_{xc}[\rho] \tag{2.4}$$

T_S represents the kinetic energy of a system of non-interacting electrons as a functional of the density $\rho(\mathbf{r})$, the second term is the classical Coulomb repulsion, the third term is the interaction with the lattice potential and E_{xc} the exchange and correlation energy including all the non-classical contributions. Again, the energy can be minimized by application of the variational principle, leading to the Euler-Lagrange equation 2.5.

$$\begin{aligned} \mu &= v_{eff} + \tfrac{\delta T_S[\rho]}{\delta \rho(\mathbf{r})} \\ v_{eff} &= v(\mathbf{r}) + \int \tfrac{\rho(\mathbf{r}')}{|\mathbf{r}-\mathbf{r}'|} d\mathbf{r}' + \tfrac{\delta E_{xc}[\rho]}{\delta \rho(\mathbf{r})} \end{aligned} \tag{2.5}$$

In calculations, one uses the Kohn-Sham equations in the orbital form (equations 2.6), which resemble the Hartree-Fock equations but include an effective potential containing the exchange and correlation potential instead of simply using the potential without explicitly including a correlation part.

$$\begin{aligned} (-\tfrac{1}{2}\nabla^2 + v_{eff}(\mathbf{r}))\phi_i &= \epsilon_i \phi_i \\ \rho(\mathbf{r}) &= \sum_{i=1}^{N} \sum_{s} |\phi_i((r), s)|^2 \end{aligned} \tag{2.6}$$

These equations are exact and can be solved self-consistently. Still, it is important to note that the Kohn-Sham orbital wave functions ϕ_i in general do not represent the physical orbitals of the material. Thus, also the corresponding orbital eigenvalues cannot be interpreted as the exact orbital energy; nevertheless they are sometimes used as approximate values for the eigenenergies.

2.1.2 Realization of Electronic Structure Calculations

As mentioned before, the Kohn-Sham equations are exact and suitable to perform electronic structure calculations. However, in practical calculations, the exact exchange correlation potential v_{xc} is not known and needs to be approximated.

Approximations for v_{xc}

One frequently used approximation is the *local density approximation* (LDA), which assumes that the exchange-correlation term can be locally approximated by the exchange and correlation energy of a uniform electron gas of the given density. The approximation can be improved by including local changes of the density, leading to the *generalized gradient approximation* (GGA). Usually, this significantly improves the accuracy of both, exchange and correlation energy. However, in certain cases LDA calculations can yield better results than those using GGA. Equation 2.7 shows the general form of the exchange correlation energy in GGA.

$$E_{xc}^{\mathrm{GGA}}[n_\uparrow, n_\downarrow] = \int \mathrm{d}^3 r f(n_\uparrow, n_\downarrow, \nabla n_\uparrow, \nabla n_\downarrow) \tag{2.7}$$

In order to increase accuracy further, higher order derivatives of the density can be included (meta-GGA).
Another approach, which is more frequently used, is to introduce hybrid functionals for the exchange correlation energy. In a typical hybrid functional the exchange energy of GGA is partially replaced with the exact exchange energy (Hartree-Fock exchange energy) of the overlap of the orbital wave functions. However, it should be noted that more

sophisticated approximations of the exchange correlation energy require more computational effort and should therefore only be used if high accuracy has to be achieved.

Basis Set and Pseudopotentials

For practical calculations, it is useful to expand the Kohn-Sham wave functions as series of basis functions. Since free electrons are represented by plane waves, they are a common choice for simple calculations. A plane wave basis has several advantages, such as orthogonality and simple Fourier transforms. The form of a plane wave expansion in a periodic potential is given in equation 2.8, where $\mathbf{G}$ represents a reciprocal lattice vector.

$$\phi_i = \sum_{\mathbf{G}} c_{i\mathbf{k}}(\mathbf{G}) \exp^{i(\mathbf{G}+\mathbf{k})\mathbf{r}} \tag{2.8}$$

For an accurate description of a system, infinitely many reciprocal lattice vectors would have to be included. In practice, a cut-off energy determining the number of plane waves considered in the calculations is introduced. For simple potentials, the calculations can be performed in a plane wave basis, but more complicated problems require a very large basis set; therefore different approaches are needed. Basically two methods can be applied: the first one is to choose a different basis set, the second one is to introduce pseudopotentials.

The basic idea of pseudopotentials is to simplify the calculation by replacing the exact potential by an effective potential in order to reduce the size of the basis set. In the so-called frozen core approximation, core electrons are represented by states determined in atomistic calculations and only the valence electrons' wave functions have to be calculated. In this approximation, the core states do not contribute to the bonding, but nevertheless they can change during the calculation in order to achieve orthogonality to the valence states. In the core region, the valence electrons interact with a simplified potential constructed to reproduce the correct charge density and eigenvalues. Outside the core region however, the valence electrons are subject to the exact potential. The pseudopotential has to be constructed in a way that the wave functions are smooth at the boundary of the core region.

The two approaches to simplify calculations can be generalized to methods using a pseudopotential and a different basis set. One of these methods is employed in the calculations in the present diploma thesis. It is based on the *projector augmented wave* (PAW) method [4] introduced by Blöchl in 1994 and uses the PBE ([5],[6]) functional, a functional of GGA-type. In the following paragraph the basic principles of the PAW method are explained on the basis of [4].
In augmented wave-methods, such as the PAW method, the lattice site is divided into two parts: one in the so-called augmentation region around the core, where the wave function can exhibit strong oscillations, the other one in the interstitial region. The oscillations in the core region can lead to very involved calculations; therefore in the PAW method further steps are applied. Blöchl introduces a pseudo-Hamiltonian with simpler eigenstates in the augmentation region under the condition that a linear transformation between the physically relevant Hilbert space of the Hamiltonian of the problem and the Hilbert space of the pseudo-Hamiltonian exists. Hence the calculations inside the augmentation region can be performed for the pseudo-Hamiltonian. The solution in the pseudo-Hamiltonian's space is represented by an expansion into partial waves $\tilde{\phi}_i$, which can be transformed to partial waves ϕ_i of all-electron calculations (determined in atomistic calculations) in the physical space using the linear transformation between the two spaces (see equation 2.9). Since the transformation is linear, the expansion coefficients are the same for both spaces.

$$\begin{aligned} \mid \Psi\rangle &= \sum_i c_i \mid \phi_i\rangle \\ \mid \tilde{\Psi}\rangle &= \sum_i c_i \mid \tilde{\phi}_i\rangle \end{aligned} \tag{2.9}$$

To ensure the correctness of the calculations, the partial waves $\tilde{\phi}_i$ have to coincide with their counterpart ϕ_i outside the augmentation region, in which the transformation is valid. The components of the valence electrons' wave function as they can be written in the PAW method are illustrated in equation 2.10.

$$\mid \Psi\rangle = \mid \tilde{\Psi}\rangle + \sum_i c_i(\mid \phi_i\rangle - \mid \tilde{\phi}_i\rangle) \tag{2.10}$$

The wave function is given by the solution of the pseudo-Hamiltonian plus the difference of the radial behaviour of the atomistic wave function and the pseudo-wave function

inside the augmentation region. This division into three parts also holds for the total energy and the charge density.
The major advantage of this method is that the energy minimization can be performed by varying the coefficients of the solution of the pseudo-Hamiltonian and subsequently transforming the wave functions to the physical solutions of the system.

Vienna ab-initio Simulation Package

The ab-initio calculations in the work were performed using VASP (*Vienna ab-initio Simulation Package*) [7], [8], [9], [10].
VASP is a Fortran program package for ab-initio calculations based on *Density Functional Theory*. Besides calculating the ground state for a given configuration, VASP can also calculate the forces acting on the ions and the stress tensor, which can be used to relax the structure to its energetic minimum. The input files necessary for VASP calculations are called INCAR, POSCAR, POTCAR, and KPOINTS. These contain all the information needed for computations.
VASP produces several output files, of which in the present work only OUTCAR will be discussed briefly.

INCAR Essentially, the parameters in INCAR determine the type of the calculation and its accuracy and precision. Furthermore, one can control which output files should be produced and if the computation should start from results of previous ones. There is a wide variety of parameters, which can be set in INCAR, but many of them have reasonable default values and need not be set explicitly. An example of an INCAR file is given in figure 2.1.2.

In the example three tags determine the type of calculation: *ALGO = Fast* determines the algorithm used for the computation, *IBRION = -1* sets up a static calculation (without relaxation of the ionic system) and because of *ISPIN=2* the calculation is spin-polarized. The other tags modify the calculation in different ways. *ENCUT* sets the energy cut-off (in eV) of basis functions included in the calculation. *NSW* gives the maximum number of ionic steps performed in a relaxation; therefore it is set to zero in the static case. *MAGMOM* initializes the total magnetic moment of the atoms in the lattice. It can be used to facilitate the convergence to a magnetic state. *LORBIT* controls if and in how much detail certain output files are produced.

```
System = Fe3Ni
ENCUT = 450
ALGO = Fast
IBRION = -1
NSW = 0
ISPIN = 2
MAGMOM = 3.5 3.5 3.5 2.5
LORBIT = 11
```

Figure 2.1: Typical INCAR file used in the present work

POSCAR POSCAR contains the information about the positions of the atoms in the material. It consists of the lattice constant, the basis vectors of the structure, the number of atoms of each type, and their positions in the basic cell. The positions can be given in Cartesian coordinates or in those of the basis of the structure.

POTCAR POTCAR files contain a pseudopotential for a given atomic species. For each element, there are several different POTCAR files available, which can be selected according to the requirements of the calculation. To construct a POTCAR file for the desired calculation, one joins the selected POTCAR files of the different atoms to one file, in the same sequence as the atomic species are listed in POSCAR.

KPOINTS The file KPOINTS determines the grid of k-points used in the computation. One possibility is to enter the desired number of k-points in each direction determining the density of the k-point mesh and let VASP generate the grid automatically in a given scheme. This method is usually applied but for example for a band structure calculation along specific directions KPOINTS can consist of explicit coordinates.

OUTCAR Most of the important information about the computation and its results is written to the OUTCAR file. Besides computational details for each iteration step and an analysis of the calculated system, OUTCAR contains detailed information on the system's energy, the forces acting on the atoms, and the magnetic moments for each atom, orbital and direction (for non-collinear calculations).

2.2 Thermal Expansion

In physics, temperature is always associated with movement of particles. In the solid state, lattice vibrations, phonons, constitute the major contribution to the thermal energy. For many calculations in solid state physics, it is sufficient to describe phonons in a harmonic approximation, in which displacement terms are included up to the second order in an expansion of the ionic pair potential.
To describe thermal expansion, anharmonic terms have to be included. These anharmonic terms modify the ionic interaction potential, causing the equilibrium distance to shift to larger values for increasing temperature. In addition to a change in equilibrium volume owing to the anharmonicity of the potential, higher temperatures also lead to more and higher excitations of phononic normal modes. One can establish a connection between the equilibrium volume and the phonon frequencies in the crystal via the temperature dependence of the two quantities. This relation is described by the Grüneisen parameter $\gamma_{\mathbf{k}s}$ as defined in equation 2.11 [11]. The weighted average of all modes **k**,s weighted with their contribution to the specific heat $c_{vs}(\mathbf{k})$ results in the overall Grüneisen parameter γ.

$$\gamma_{\mathbf{k}s} = -\frac{V}{\omega_s(\mathbf{k})}\frac{\partial\omega_s(\mathbf{k})}{\partial V} \tag{2.11}$$

To describe thermal expansion, one defines a parameter α which directly relates the equilibrium volume with the temperature (see equation 2.12 [11]), where $B = -V\left(\frac{\partial P}{\partial V}\right)$ represents the bulk modulus.

$$\alpha = \frac{1}{l}\left(\frac{\partial l}{\partial T}\right)_P = \frac{1}{3V}\left(\frac{\partial V}{\partial T}\right)_P = \frac{1}{3B}\left(\frac{\partial P}{\partial T}\right)_V = \frac{\gamma c_v}{3B} \tag{2.12}$$

Examining the terms more closely, it can be made plausible that the left hand side in equation 2.12 represents the relation between volume and temperature:

- The bulk modulus relates the pressure to the equilibrium volume,
- γ relates the equilibrium volume to phononic modes,

- the specific heat gives the connection between the phonons and temperature

For a derivation of this relation, see for example [11].
This form of the thermal expansion coefficient containing γ, c_v, and B clearly demonstrates the different effects influencing thermal expansion. Especially at low temperatures, the temperature dependence of α and c_v can be very similar, whereas for other materials γ can become negative and lead to negative thermal expansion over a certain temperature range [12].
While equation 2.12 only considers the phononic part of the thermal expansion, in metals electrons can also contribute a considerable part to the thermal expansion. At low temperatures the electronic contribution can be of the same order than the phononic part, so that equation 2.12 must be modified, resulting in equation 2.13 [11].

$$\alpha = \frac{1}{3B}(\gamma c_v^{ion} + \frac{2}{3}c_v^{el}) \tag{2.13}$$

2.2.1 The Invar Effect

Since in 1897 Guillaume discovered the remarkable fact that Fe-Ni alloys of certain compositions exhibit almost no thermal expansion over a wide temperature range [1], various other alloys have been discovered showing this behaviour, known as the Invar effect. With increasing number of Invar materials, one discovered that the behaviour is neither restricted to certain crystal structures nor to binary alloys. Even amorphous and multi-component systems can exhibit this anomaly in thermal expansion.
Since materials with virtually no thermal expansion are interesting for various applications, such as length standards, precision instruments or industrial molding tools, the discovery led to increased efforts in Invar materials research. Numerous attempts have been made to explain this phenomenon with a theory matching the experimental results. As a first step, in order to describe the new behaviour one has to split the linear thermal expansion coefficient into a term representing the lattice vibrations, the source of usual thermal expansion, and an anomalous term (see equation 2.14).

$$\alpha = \alpha_{lat} + \alpha_{an} \tag{2.14}$$

The fact that all other Invar materials also exhibit ferro- or antiferromagnetic behaviour and a large spontaneous volume magnetostriction [13], obviously suggests a connection of α_{an} to the magnetic properties of the material. Today the hypothesis that Invar behaviour is closely related to magnetism is widely accepted and the large spontaneous magnetostriction is regarded as an essential property of all Invar materials. Further noticeable characteristics of the Invar anomaly are, amongst others, the following [13]:

- Large negative pressure effects on the magnetization
- Large forced volume magnetostriction
- Anomalous temperature dependence of elastic constants

Regarding all the different anomalies occurring in a variety of materials and structures, it is clear that the requirements for a theory explaining the Invar effect are high. This might be the reason why more than 120 years after the discovery of the effect, no microscopic theory which agrees quantitatively with all experimental results has been established. In this section, the basic concept of different approaches to explain the Invar effect will be discussed on the basis of reviews by Shiga [13] and Wasserman [14].
To understand the ideas behind different models of the Invar effect, it is instructive to review two models of magnetism, both of which set the basis for models of the Invar effect.

Localized Magnetic Moments

In a very general quantum mechanical approach, local moments are described by the Heisenberg Hamiltonian, which treats the spins on the lattice sites as quantum mechanical observables with pairwise interaction. Including the interaction with an external field, the Heisenberg Hamiltonian is given by equation 2.15 [15].

$$\widehat{H} = -I_h \sum_{l,\delta} \widehat{\mathbf{S}}_l \widehat{\mathbf{S}}_{l+\delta} - g_j \mu_B H_{ext} \sum_l \widehat{S}_{zl} \tag{2.15}$$

The sum over l represents all the lattice sites and δ selects the interaction partner of the spin at the site l. The material-specific quantity I_h is called exchange integral

and represents the strength of the interaction between two spins. It is positive for ferromagnetic and negative for antiferromagnetic coupling. In the ground state, the spins are aligned parallel to the nonzero external field H_{ext}.
The solutions of the Heisenberg Hamiltonian represent the magnetic state of the system. The excited states are bosonic excitation modes of the spin system called magnons or spin waves.
One simple example of an approximation to the Heisenberg model is the Ising model. In this strongly simplified model the spin operators are replaced by their z-components, leaving only two possible states (spin up and spin down) for each lattice site.
Based on a simplified model Shiga [13] shows that the model of localized moments fails to reproduce the non-zero forced magnetostriction coefficient at zero temperature. Furthermore, the magnetism in transition metals cannot be explained with the model of localized magnetic moments. For these reasons, the theory of localized magnetic moments alone cannot provide a quantitative explanation of the Invar effect.

Itinerant Electron Model

The concept of itinerant electron magnetism was introduced by Stoner [16]. In the Stoner model, the unsaturated electron spins in d-bands are responsible for magnetism. In contrast to the previous model, the electrons are no longer localized at the lattice sites but they can move in the periodic lattice potential. Furthermore, magnetic moments can take values of non-integer multiples of μ_B.
A molecular field representing the exchange effects causes a higher population of the band in one spin direction, corresponding to a spin dependent energy shift of the highest occupied state. The molecular field per atom H_M and the corresponding energy shift ϵ_m are given by equation 2.16 [15], where M is the absolute and ζ the relative magnetization and N is a constant relating the magnetization to the molecular field. Θ represents a characteristic temperature for the magnetic energy.

$$\begin{aligned} H_M &= NM = NM_0\zeta, && \text{with } \zeta = \tfrac{M}{M_0} \\ \epsilon_m &= -\mu_B H_M = -\mu_B N M_0 \zeta = -k_B \Theta \zeta, && \text{with } \Theta = \tfrac{\mu_B N M_0}{k_B} \end{aligned} \tag{2.16}$$

In the same way as an external field applied to a paramagnet, the molecular field causes the density of states to lose its symmetry for spin up and down. The spin direction

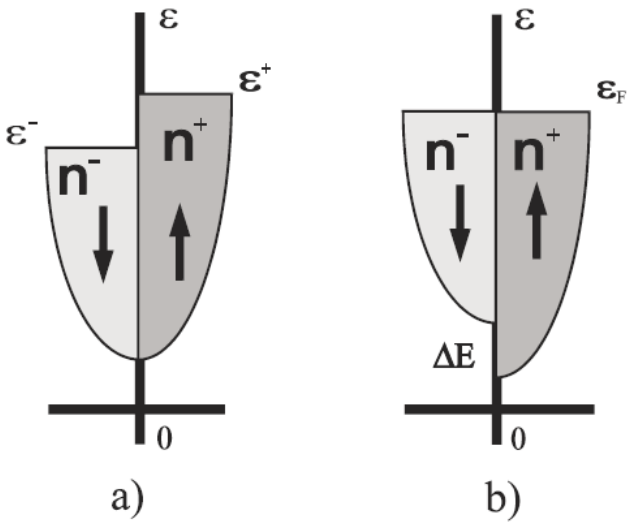

Figure 2.2: Two representations of the spin split density of states, $n^{\pm}$ represents the number of electrons with spin up/down, $\varepsilon^{\pm}$ the corresponding Fermi energy. [15]

parallel to the molecular field is energetically favourable and so the electrons preferably occupy states in this direction. This alignment parallel to the field leads to a gain in magnetic energy but it also costs kinetic energy, because the electrons have to populate higher states owing to the Pauli Exclusion Principle. In figure 2.2 two possible interpretations of the spin splitting are illustrated. In 2.2a) the molecular field causes a shift in the Fermi energies of the two spin orientations, whereas in figure b) the lowering of the energy of the spin-up band is emphasized. In figure b) it is evident that the system is in equilibrium, because it is clear from the figure that the chemical potentials for both spin states are equal. The figure also illustrates that a high density of states at the Fermi energy favours a larger magnetization, because the electrons changing the spin direction need less additional kinetic energy.

Using the condition that for ferromagnetic ordering the energy has to have a maximum at $\zeta = 0$ (no magnetization), the calculation of the energy and its extrema yields the Stoner criterion for spontaneous magnetic ordering [15]:

$$\frac{2}{n}\mathcal{N}(\varepsilon_F)k_B\Theta \geq 1 \tag{2.17}$$

In equation 2.17, n represents the number of electrons. The equation demonstrates that

a large density of states at the Fermi energy and a large characteristic temperature (meaning large values of N and M_0) favour ferromagnetic order.
Depending on the occupation of the spin bands in the ferromagnetic state, one can distinguish strong and weak ferromagnets. In a strong ferromagnet, one spin band is completely filled. Thus an increase of the field does not lead to a significant change of the magnetic moment. If neither of the spin bands of a ferromagnet is completely occupied, the material is called weakly ferromagnetic.
In [13] Shiga states that for certain forms of densities of state (a sharp peak above the paramagnetic Fermi level) and appropriate Θ, it is possible to realize two energy minima in dependence of the magnetization, a high spin and a low spin state. The importance of this observation will become clear in the discussion of the models of the Invar effect. Furthermore, Shiga explains the effects of spin fluctuations as an extension of the theory of itinerant electrons. By including spin fluctuations one can retain a finite local spin density above the Curie temperature as dynamic spin fluctuations in contrast to the Stoner model, in which the magnetic moments vanish completely above T_c.

Models of the Invar effect

In a review of the Invar effect [14], Wasserman points out the diversity of theories trying to explain the characteristics of Invar. Given the wide variety of models, in the present diploma thesis only a selection of models important for Fe-Ni alloys will be discussed.
Wasserman briefly discusses the model of latent antiferromagnetism, a model based on local moments, which was published in its first form in 1960 by Kondorsky and Sedov [17]. This model explains the Invar anomaly with a negative exchange integral of the d-electrons in Fe in the fcc phase, resulting in antiferromagnetic coupling for certain concentrations and in the coexistence of parallel and antiparallel regions near a critical concentration. The critical concentration is determined by the values of the exchange integrals Fe-Fe, Fe-Ni, and Ni-Ni, of which only Fe-Fe is assumed to be negative. In order to make the antiferromagnetic coupling in the fcc-phase of the Fe-Ni system plausible, Kondorsky and Sedov refer to other alloys of Fe in the fcc-phase exhibiting antiferromagnetism (for example FeMn with more than 12% Mn).
The idea of the coexisting parallel and antiparallel moments was revisited in 1976 by Jo [18]. Jo performed concentration dependent calculations of Fe-Ni systems in coherent potential approximation, describing the atoms in an effective medium given by a coherent

potential. He found two solutions (parallel and antiparallel moments) and determined the vanishing of the energy difference as condition for the critical concentration, where they can coexist. However, he was unable to reproduce the significant decrease of magnetization near $Fe_{65}Ni_{35}$.
In 1963 Weiss [19] proposed that the Invar effect in Fe-Ni alloys resulted from a transition between two different electronic configurations of iron atoms in a fcc lattice. In this so-called 2γ state model, Weiss starts from the fact that in γ iron additionally to the antiferromagnetic ground state a ferromagnetic state with larger volume exists. Weiss suggested that alloying iron with a sufficient amount of nickel can stabilize the ferromagnetic ground state with larger volume at zero temperature. With increasing temperature, thermal excitation of the state with the smaller volume can partially compensate the normal thermal expansion originating in the anharmonicity of the ions' potential.
Although the existence of these states in Fe-Ni Invar alloys has never been proven experimentally, the basic idea of two states with a high and a low magnetic moment found new support around 1990, when first principles studies discovered the existence of two energetic minima at different volumes. Moruzzi [20] carried out fixed spin moment calculations at different volumes and found that in Fe_3Ni, for a certain volume, the ferromagnetic high-spin-state and a low-spin-state are in equilibrium. The volume dependence of the two states found by Moruzzi is illustrated in figure 2.3. The common tangent line in the figure represents the pressure, at which high-spin and low-spin states are in equilibrium. Another remarkable fact found by Moruzzi is the small energy difference between the two states (about 1 mRy). Moruzzi referred to the high spin and low spin states in Fe_3Ni as the "band-theoretical equivalent of the 2γ states proposed by Weiss" [20]. Antiferromagnetic Invar materials are supposed to exhibit a similar behaviour but with an antiferromagnetic ground state instead of the ferromagnetic high spin state. From Moruzzi's ab-initio calculations and similar ones for different Invar materials, one can reproduce essential ground state properties of Invar alloys.

Finite Temperature Models

Since neither of the theories mentioned above can reproduce the temperature dependence of the Invar materials' properties correctly, one needs more elaborate theories for finite temperature descriptions.
The most frequently used approach to finite temperature modelling is spin fluctuation

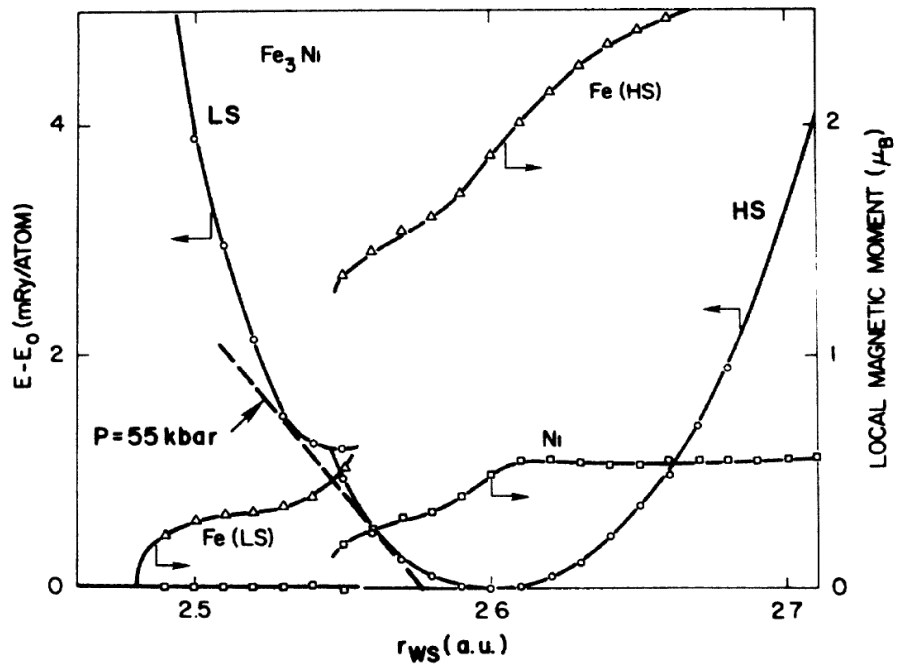

Figure 2.3: Total energy and magnetic moment of Fe, Ni and Fe_3Ni as a function of the volume (Wigner-Seitz radius) [20]. HS=high spin, LS=low spin

theory in all its varieties. Hasegawa [21] calculated the temperature dependence of the square spin fluctuation amplitude and was able to explain the large spontaneous magnetostriction and other properties of Invar alloys. In his calculations, Hasegawa introduces a coherent potential depending on random exchange fields at lattice sites. The mean values of these exchange fields represent the local moments. Since further details of these calculations are rather complex and not relevant for the understanding of the present work, they will be omitted.

In addition to developing different spin fluctuation approaches, Kakehashi [22] introduced a theory of local environment effects, which he employed in the calculation of the concentration dependence of the local moments of Fe and Ni. In principle, this theory is similar to the molecular field approach but it includes interactions of local variations of the field with the environment. The thermal average of a local moment at a lattice site is given by the classical average of a field variable at this position. The energy expression used for this average includes in zeroth order only the interaction with an effective medium, representing the overall average of the potentials and spin fluctuations. The first order deviation from the effective medium is given by the energy contribution of the local field variables at the lattice sites. Finally, the second order correction constitutes of

the pairwise interaction of the local field variables. In this model only nearest-neighbour contributions are considered and the field variables are replaced by effective Ising spins given by their thermal average (local moments). Thus, local fluctuations contribute an important part to the total behaviour of the system. Using this approach, one can calculate distributions of the local moments and their amplitudes at different temperatures and for different concentrations. It is important to note that this theory of local environment effects is a static approximation.

Another approach follows a Ginzburg-Landau mean field theory of spin fluctuations developed by Wagner [23]. The basics of this phenomenological method of including fluctuations will be explained in more detail in section 2.3.1, since it is employed in the present diploma thesis in a similar form. Mohn et al. [24], [25] applied this theory to Fe_3Ni, starting from the energy surface, a polynomial function in two variables $E(M, V)$ fitted to results of a fixed spin moment calculation. An important characteristic of this approach is that besides the fluctuations of the magnetic moment also volume fluctuations are included.

In more recent publications, temperature dependence is often taken into account using the disordered local moment (DLM) formalism [26]. In DLM calculations one assumes the existence of local magnetic moments at each site. The local moments of an atomic species are divided into spin-up an spin-down contributions, which are treated like two components of a random alloy. The computational realization, as it was introduced for example by Gyorffy [26], is based on a spin-density functional description of an inhomogeneous interacting electron liquid. In the DLM picture, one assumes the existence of a molecular field and calculates the temperature dependent magnetization from statistical mechanics. In contrast to a simple Curie-Weiss picture, the molecular field in the ground state is provided by ab-initio calculations in local spin density approximation. In more advanced versions of DLM, the mean-field is replaced by more elaborate concepts.

In 1999, Schilfgaarde et al. [27] were among the first groups to perform ab-initio calculations in local spin density approximation considering non-collinear magnetic moments. They observed that the occurrence of two energetic minima (high-spin, low-spin) in Fe-Ni alloys used in many models before is just a consequence of the constraint to collinear magnetism. In the ground state they found a continuous transition from the ferromagnetic state at large volumes to disordered non-collinear states for smaller cells. The transition starts at higher volumes than the transition high-spin to low-spin and the average magnetization changes much faster than the average values of local moments of Fe and Ni. Since this model gives good agreement with many experimental values,

it led to experiments trying to find non-collinear states. However, these experiments (e.g. [28] using neutron scattering with polarization analysis) did not find evidence for non-collinear ferromagnetism in Fe-Ni Invar.

Further investigations of Invar characteristics

In [29] Entel et al. include structural considerations into the discussion of the Invar effect. In band structure calculations of the Invar model system Fe_3Ni in the $L1_2$ structure the authors concentrate on the t_{2g} and e_g states of majority and minority spin bands. In the high moment state Entel et al. found that near the Fermi energy the majority spin t_{2g} antibonding orbital and the minority spin e_g non-bonding orbital are energetically close. This suggests that with rising temperature a charge transfer from the majority spin t_{2g} antibonding to the minority spin e_g non-bonding occurs, leading to a decrease in volume. Furthermore, the effects of tetragonal distortions of the cubic lattice on the crystal field orbitals are analysed. Their results suggest that a tetragonal distortion causes a band shift that could also lead to a shrinking of the lattice counteracting the thermal expansion.

The spontaneous magnetostriction as a characteristic of the Invar effect in different Fe-compounds is the topic of a publication by Khmelevskyi et al. [30]. Comparing the ferromagnetic state to the paramagnetic DLM state, the spontaneous magnetostriction was calculated. It was found that the spontaneous magnetostriction reaches its maximum value approximately at the valence electron number of 8.5 electrons per atom, corresponding to the highest difference of the magnetic moments of the ferromagnetic and the paramagnetic DLM state. Since this valence electron number is typical for ferromagnetic Invar compounds, this result gives a connection between the Invar effect and large changes in the local magnetic moments.

One of the most important questions remaining unanswered is whether the physical mechanisms leading to Invar behaviour in Fe-Ni alloys are the same as in other materials. Given the fact that the Invar effect is not constrained to materials with a specific structure, especially the role of structural transformations, one of which occurs near the Invar region in Fe-Ni Invar and other Invar alloys, gives rise to this question.

The Invar System $Fe_{65}Ni_{35}$ and its model systems

The original Invar alloy $Fe_{65}Ni_{35}$ is a disordered ferromagnetic alloy with an fcc-like structure. At room temperature its equilibrium lattice constant is a=3.595 Åand its thermal expansion coefficient is $\alpha < 2 \cdot 10^{-6} K^{-1}$ [13]. At low temperatures, its magnetic moment per atom is 1.77 μ_B/atom and the spontaneous magnetostriction is estimated to $\omega_s(0) = 1.8 \cdot 10^{-2}$ [13].
Since ab-initio calculations usually use periodic boundary conditions, they do not support random distribution of the atomic species; hence calculations for this system would require very large cells. Therefore the calculations are performed for ordered model systems. The most common model system for Fe-Ni Invar is Fe_3Ni, which is also used in the present diploma thesis. Fe_3Ni also is a disordered alloy, but for the calculations it is assumed to have Cu_3Au ($L1_2$) structure. In order to simulate different concentrations, the calculations are also performed for an artificial Fe_5Ni_3 cell. For this composition, the Fe_3Ni cell described above is doubled in z-direction and the central Fe-atom is replaced with a Ni-atom. The two model cells are depicted in figure 2.4.

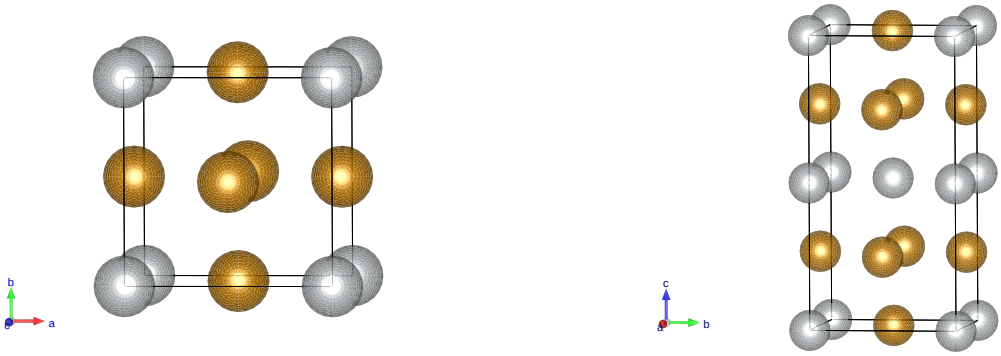

Figure 2.4: $L1_2$ structure of Fe_3Ni cell (left); Fe_5Ni_3 cell (right). Grey balls represent Ni-atoms, golden balls Fe-atoms.

The magnetic and structural properties for different concentrations of Ni can be found in the phase diagram in figure 2.5. The hatched regions are the regions of Invar and of the martensitic transformation. The solid lines represent the concentration dependence of the Curie temperature and the magnetic moment. The dashed line describes the concentration dependent equilibrium volume per atom given in terms of the Wigner-Seitz radius.

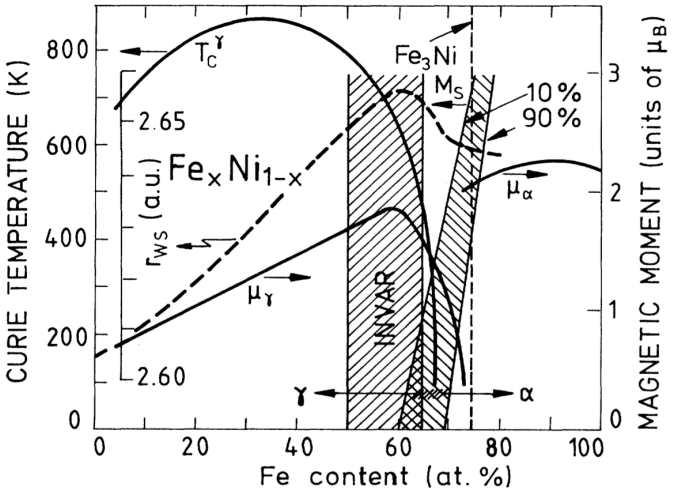

Figure 2.5: Structural and magnetic phase diagram of Fe-Ni-alloys.[29]

2.3 Fluctuations of Thermodynamical Variables

A macroscopic system in equilibrium is characterized by physical quantities which are always close to their average values. But in every system, these quantities show small deviations from their average values; they fluctuate. In order to describe the system correctly, one needs to specify the distribution of the fluctuations.
In [31], the distribution of the fluctuating values of a variable x around its average value $\overline{x} = 0$ is derived. One argues that for temperatures and times, for which quantum fluctuations can be neglected, the probability distribution of the energies of a system as a function of the entropy is given by equation 2.18, corresponding to the Boltzmann formula.

$$w(x) = const \cdot e^{S(x)} \tag{2.18}$$

Since the entropy is maximal for the equilibrium value of x, the conditions given in equation 2.19 can be used to determine an expression for the entropy.

$$\left(\frac{\partial S(x)}{\partial x}\right)_{x=0} = 0, \qquad \left(\frac{\partial^2 S(x)}{\partial x^2}\right)_{x=0} < 0 \tag{2.19}$$

In the simplest case, the expansion of S(x) into a series fulfilling these conditions is given by equation 2.20.

$$S(x) = S(0) - \frac{\beta}{2}x^2 \tag{2.20}$$

Together with equation 2.18, this leads to a Gaussian form for the probability distribution of x. Normalizing the probability distribution ($\int w(x)dx = 1$) results in equation 2.21 [31].

$$w(x)dx = \sqrt{\frac{\beta}{2\pi}}e^{-\frac{\beta}{2}x^2}dx \tag{2.21}$$

Knowing the distribution function, one can calculate the statistical averages of all powers of the fluctuations. Since the Gaussian distribution is symmetric, the averages of odd powers of x vanish. The average of even powers of x is given by equation 2.22 [15].

$$\langle x^{2k}\rangle = \int x^{2k}w(x)dx = \beta^{-k}\cdot(2k-1)!! = \langle x^2\rangle^k\cdot(2k-1)!! \tag{2.22}$$

Also fluctuations of more than one variable can be represented by a Gaussian distribution. These variables are regarded as independent if averages of mixed terms vanish ($\langle x_i x_j\rangle = \delta_{ij}$). For example in [31], it is demonstrated that fluctuations of entropy and pressure (or correspondingly temperature and volume) are independent.

2.3.1 Ginzburg-Landau Model for Fluctuations

Wagner [23] developed a Ginzburg-Landau model including fluctuations of both variables, magnetic moment and volume. Wagner's theory is a generalization of the theory of Murata and Doniach [32], who were the first to develop a mean-field theory of fluctuations of the magnetic moment.
Starting from a polynomial representing the energy surface at zero temperature, which is determined in static ab-initio calculations, the fluctuations introduce temperature to the system. In a similar way, this formalism can be rewritten for fluctuations of the c/a-ratio of a bct (body-centered tetragonal) cell and the volume per atom in order

to describe structural transformations, as it is performed for example in [33]. Since in the present diploma thesis the relevant variables are the c/a-ratio and the volume, the derivation will be presented for these variables based on [33], [23] and [15].
The energy surface $E(c/a, V)$ at zero temperature is represented by a polynomial in two variables (equation 2.23). The coefficients of the polynomial are calculated by fitting the function to data points of an energy surface obtained in static ab-initio calculations. In the next step, the variables are replaced by the statistical average over the equilibrium value plus the corresponding fluctuation: $c/a \to \langle c/a + \xi(r) \rangle$ and $V \to \langle V + \nu(r) \rangle$.

$$E(c/a, V) = \sum_{i=0}^{n} \sum_{j=0}^{m} A_{ij} (c/a)^i V^j \tag{2.23}$$

First, the binomials $(c/a + \xi(r))^i$ and $(V + \nu(r))^j$ are evaluated, then the average values are calculated, using equation 2.22. Thus the only fluctuation terms occurring in the expression for the energy are amplitudes ($\langle \xi^2 \rangle, \langle \nu^2 \rangle$). The energy is now a function of four variables: V, c/a, $\langle \xi^2(r) \rangle$, and $\langle \nu^2(r) \rangle$, the fluctuation terms being random, non-centred variables. Furthermore, the length scale of the variation of the fluctuations is assumed to be larger than the range of interactions. Accounting for the spatial dependence of the fluctuations by introducing lowest order gradient terms leads to the Hamiltonian of the system (equation 2.24) [33].

$$H = \frac{1}{V} \int d^3r \left[E(c/a + \xi(r), V + \nu(r)) + \frac{K}{2} (\nabla \xi(r))^2 + \frac{Q}{2} (\nabla \nu(r))^2 \right] \tag{2.24}$$

The gradient terms strongly suppress large short-range fluctuations. The coefficients K and Q determine the width of the distribution of fluctuations in the k-space. Mohn et al. [33] refer to K and Q as stiffness constants, in analogy to the spin-wave stiffness in magnetic systems.
Furthermore, one introduces a variable ϕ (equation 2.25) representing the energy contribution of the fluctuations.

$$\phi = \frac{1}{V} \int d^3r \left[E(c/a + \xi(r), V + \nu(r)) - E(c/a, V) \right] \tag{2.25}$$

In order to calculate the free energy, the partition function (Z) needs to be calculated,

involving an integration over the phase space of the fluctuations (Γ).

$$F = -k_B T \ln Z, \qquad Z = \int d\Gamma e^{-\beta H}, \qquad \text{with } \beta = \tfrac{1}{k_B T} \tag{2.26}$$

In general, the functional integral cannot be calculated; therefore an approximation needs to be applied. The approximation of the free energy is obtained using the Peierls [34] - Feynman [35] inequality (equation 2.27) and minimizing the right hand side of the equation.

$$F \leq F_0 + \langle H - H_0 \rangle_0 \tag{2.27}$$

F_0 represents a trial free energy calculated from the trial Hamiltonian H_0, which is chosen in a very general form. $\langle \cdots \rangle_0$ describes the statistical average of the given quantity using the approximate partition function. The full calculation is performed for magnetic fluctuations in [15]. The resulting expressions for the free energy and the mean square fluctuations are given by equations 2.28 and 2.29.

$$\begin{aligned} F = E(c/a, V) + \quad & \phi(c/a, V, \langle \xi^2(r) \rangle, \langle \nu^2(r) \rangle) \\ & - \frac{k_B T}{2} \sum_{k \leq k_c} \ln \frac{\pi k_B T}{2((K/2)k^2 + \partial\phi/\partial\langle \xi^2(r) \rangle)} - \langle \xi^2(r) \rangle \frac{\partial \phi}{\partial \langle \xi^2(r) \rangle} \\ & - \frac{k_B T}{2} \sum_{d \leq q_c} \ln \frac{\pi k_B T}{2((Q/2)k^2 + \partial\phi/\partial\langle \nu^2(r) \rangle)} - \langle \nu^2(r) \rangle \frac{\partial \phi}{\partial \langle \nu^2(r) \rangle} \end{aligned} \tag{2.28}$$

$$\begin{aligned} \langle \xi^2(r) \rangle &= \frac{V}{(2\pi^3)} \frac{k_B T}{2} \int_0^{k_c} \frac{4\pi k^2}{((K/2)k^2 + \partial\phi/\partial\langle \xi^2(r) \rangle)} dk \\ &= \frac{V}{2\pi} \frac{k_B T}{K} \left(k_c - \sqrt{\frac{\partial\phi/\partial\langle \xi^2(r) \rangle}{K}} \cdot \arctan\left(\sqrt{\frac{K}{\partial\phi/\partial\langle \xi^2(r) \rangle}} k_c \right) \right) \\ \langle \nu^2(r) \rangle &= \frac{V}{(2\pi^3)} \frac{k_B T}{2} \int_0^{q_c} \frac{4\pi k^2}{((Q/2)k^2 + \partial\phi/\partial\langle \nu^2(r) \rangle)} dk \\ &= \frac{V}{2\pi} \frac{k_B T}{Q} \left(q_c - \sqrt{\frac{\partial\phi/\partial\langle \nu^2(r) \rangle}{Q}} \cdot \arctan\left(\sqrt{\frac{Q}{\partial\phi/\partial\langle \nu^2(r) \rangle}} q_c \right) \right) \end{aligned} \tag{2.29}$$

The integral in equations 2.29 originates from a summation in k-space over all wavevectors. Here the assumption was made that the system is isotropic in k and in good approximation the summation can be cancelled at a finite maximum value k_c (or q_c for the volume fluctuations), the cut-off k-vector. This approximation is necessary, because otherwise the integral would not yield finite values.

Solving the integrals in equations 2.29 leads to equations for the fluctuations depending on the temperature and the partial derivatives of ϕ. Together with the equations of state (equations 2.30) for the c/a-ratio and the volume, these equations are the conditions for the equilibrium values of the fluctuations.

$$\begin{array}{rcll} \frac{\partial E}{\partial (c/a)} + \frac{\partial \phi}{\partial (c/a)} & = & 0, & V = const, \\ \frac{\partial E}{\partial V} + \frac{\partial \phi}{\partial V} & = & -P, & c/a = const \end{array} \tag{2.30}$$

Since ϕ depends on the fluctuation amplitude and vice versa, the equations have to be solved self-consistently. It is important to note that only in the ground state $E + \phi$ corresponds the physical energy surface. For finite temperatures, it is just a mathematical quantity used to calculate the equilibrium values of the fluctuations. Inserting these values into the equation for the free energy (equation 2.28) yields the physical results of the calculation. From equation 2.28 one can derive expressions for the entropy and the total energy (see equations 2.31,2.32) [33].

$$\begin{array}{rcl} S = -\frac{\partial F}{\partial T} & = & \frac{k_B}{2} \sum\limits_{k \leq k_c} \left(1 + \ln \frac{\pi k_B T}{2((K/2)k^2 + \partial\phi / \partial \langle \xi^2(r) \rangle)}\right) \\ & & + \frac{k_B}{2} \sum\limits_{k \leq q_c} \left(1 + \ln \frac{\pi k_B T}{2((Q/2)k^2 + \partial\phi / \partial \langle \nu^2(r) \rangle)}\right) \end{array} \tag{2.31}$$

Obviously, the second terms in the sums diverge for zero temperature because the expression for the entropy is based on a classical (high temperature) expansion; therefore it is not valid for temperatures close to 0 K [33]. In the calculation of the expression for the total energy (equation 2.32) the diverging terms cancel with the corresponding terms in the free energy.

$$\begin{array}{rcl} U = F + TS & = & E + \phi - \langle \xi^2(r) \rangle \frac{\partial \phi}{\partial \langle \xi^2(r) \rangle} + \frac{k_B T}{2} \sum\limits_{k \leq k_c} \\ & & - \langle \nu^2(r) \rangle \frac{\partial \phi}{\partial \langle \nu^2(r) \rangle} + \frac{k_B T}{2} \sum\limits_{k \leq q_c} \end{array} \tag{2.32}$$

In both equations there are sums without dependent variables. These sums represent the number of independent fluctuation modes considered in the calculations and give a constant contribution to the energy (at fixed temperature) and to the entropy. In terms of the specific heat, these contributions represent Dulong-Petit's law.

The temperature evolution of the system and its phase transition can be visualized in contour plots of the total energy. Since the calculations give an analytical expression for the total energy U for each temperature, the thermal evolution of many properties of the system, such as the bulk modulus, the thermal expansion coefficient, and the elastic constant C', can be derived.
The application of this method to Fe_3Ni and Fe_5Ni_3 is the topic of chapter 4.

2.4 Structural Considerations and the Martensitic Transition

An essential characteristic of Fe_3Ni is that the energy as a function of a volume-conserving tetragonal deformation $E(c/a)|_V$ exhibits two minima, corresponding to an fcc-like and a bcc-like structure. Both structures can be regarded as special cases of a body centered tetragonal (bct) cell.
The existence of minima at the bcc-like and the fcc-like structure is not a coincidence but has its foundations in the high coordination numbers of the bcc and fcc structures. It can be shown that these maxima in the number of nearest neighbours minimize the electrostatic energy. A more detailed description of the influence of the c/a-ratio on the energy is given for example in [36]. The position of the energetic minima in the energy surface $E(c/a, V)$ of Fe_3Ni is the subject of chapter 3.
The Fe_3Ni cell in the $L1_2$ structure can be regarded as a bct-like structure with a c/a-ratio of $\sqrt{2}$. After a compression of the bct cell to a c/a-ratio of 1 it corresponds to a bcc cell. One of the possible processes of this transformation, called the martensitic transformation, is illustrated in figure 2.6.

The martensitic transformation is observed in iron, where a high-temperature fcc-phase changes to a low-temperature bcc phase (called martensite). It is a diffusionless transition between these phases. In Fe-Ni alloys with high iron content, the martensitic transition is found at lower temperatures than in pure Fe. However, the transition temperature decreases with increasing Ni-concentration until the fcc-like phase becomes the stable ground state at approximately 30% Ni (see section 4.1). The simplest path relating the two phases is Bain's path [38]. It connects the bcc and fcc phases via a volume-conserving tetragonal deformation.
An analysis of Bain's path in Fe_3Ni and other materials, similar to the computations

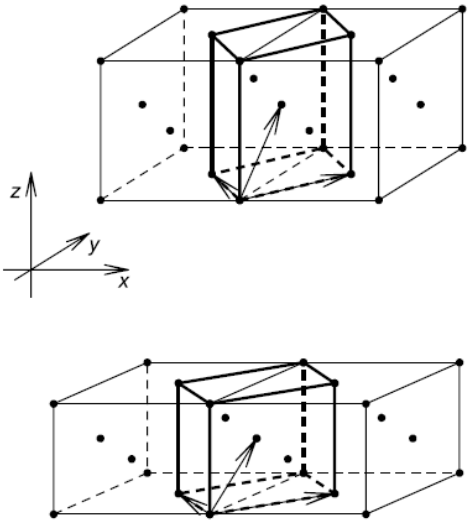

Figure 2.6: The two structures in the fcc to bcc transition. The upper figure shows an fcc cell with a bct (body centred tetragonal) cell highlighted. The lower figure illustrates the cell after the tetragonal deformation. [37]

in chapter 3, was performed by Gruner et al. [39]. Gruner et al. calculated the energy as a function of the volume and the tetragonal distortion for Fe_3Ni, Fe_3Pt, and Fe_3Pd. They investigated the structural stability of these materials by calculating the phonon dispersion relations. For each alloy, phonon softening is observed, especially in the vicinity of the M-point in k-space. The imaginary frequencies occurring in these areas due to the phonon softening mean that a static lattice deformation can lead to an energy gain.

3 Ab-initio Calculations

The first aim of the present diploma thesis is to illustrate the importance of magnetism in the martensitic transformation from the α-phase to the γ-phase of Fe_3Ni. Since the typical Invar system $Fe_{65}Ni_{35}$ occurs in a disordered state and calculations require a large cell, the system is approximated by the two model systems Fe_3Ni and Fe_5Ni_3 explained in section 2.2.1.

In order to compare the magnetic and the non-magnetic ground states, static ab-initio calculations are performed at different volumes of the unit cell for different tetragonal deformations (variations of the c/a-ratio). In all the calculations in the present work, the cell is regarded as body centered tetragonal, meaning that $c/a = 1$ corresponds to the bcc-like cell and $c/a = \sqrt{2}$ to the fcc-like structure. To examine Bain's path [38] of the martensitic transformation and the surroundings of the energetic minima, 35 c/a-ratios from 0.82 to 1.56 and 21 volumes from 9.83 $Å^3$/atom to 12.66 $Å^3$/atom are included. Since the results for the magnetic model systems are used in chapter 4, the calculations for these systems have been extended to larger volume and c/a-ratio ranges. Similar computations were performed by Gruner et al.[39]. Regarding the position of the global minimum and the shape of the energy surface, the calculations in the present work agree very well with their results. In contrast to the results presented in this section, Gruner et al. do not find a local minimum but a saddle point for the fcc-like structure. In order to explain this discrepancy, it should be noted that in the present work the local minimum is found at a slightly higher c/a-ratio than $\sqrt{2}$, which is the maximum value considered by Gruner et al.

3.1 Calculations of Fe_3Ni

3.1.1 Static Calculations

The static calculations for Fe_3Ni are performed for the collinear magnetic and the non-magnetic state. The aim is to determine the ground state of Fe_3Ni and to evaluate the size of the energy barrier of the martensitic transition.
From the results of the calculations it is clear that for all the volumes considered, the magnetic state is the ground state. With decreasing volume, the energy difference between the magnetic and the non-magnetic state decreases. Simultaneously the magnetic moment of the magnetic state decreases. This is in accordance with the existence of a state with low magnetic moments at low volumes.
Figure 3.1 illustrates the system's free energy as a function of the c/a-ratio at two different volumes: the volume that minimizes the energy of the non-magnetic state, $V = 10.35$ Å^3/atom, and the volume that minimizes the energy of the magnetic state, $V = 11.61$ Å^3/atom. For comparison, the experimental lattice constant of $Fe_{65}Ni_{35}$ given in section 2.2.1 is $a = 3.595$, which corresponds to $V = 11.61$ Å^3/atom. Figure 3.1 illustrates that for realistic equilibrium volumes the magnetic state is more favourable than the non-magnetic state independent of the c/a-ratio.
The decreasing energy difference for smaller volumes mentioned above is illustrated in figure 3.1. However, for all the volumes considered in the present work, the magnetic state remains energetically lower for any c/a-ratio.
For the non-magnetic state, the fcc-like phase clearly is the energetic minimum, whereas in the magnetic state, the minimum shifts from the fcc-like phase at small volumes to the bcc-like phase at larger volumes including the equilibrium volume. Still, in all four configurations a local minimum can be found near the other respective structure. However, the non-magnetic calculations show the second minimum at $c/a < 0.9$ instead of the bcc-like $c/a = 1$.

For both structures, the fcc-like and the bcc-like, the volume of minimum energy is found to be the same, for the given resolution of the volume. Hence, a possible structural transition is assumed to follow Bain's path. This allows to define the energy barrier as the difference between the ground state energy and the highest energy value between the two minima at a constant volume (see equation 3.1).

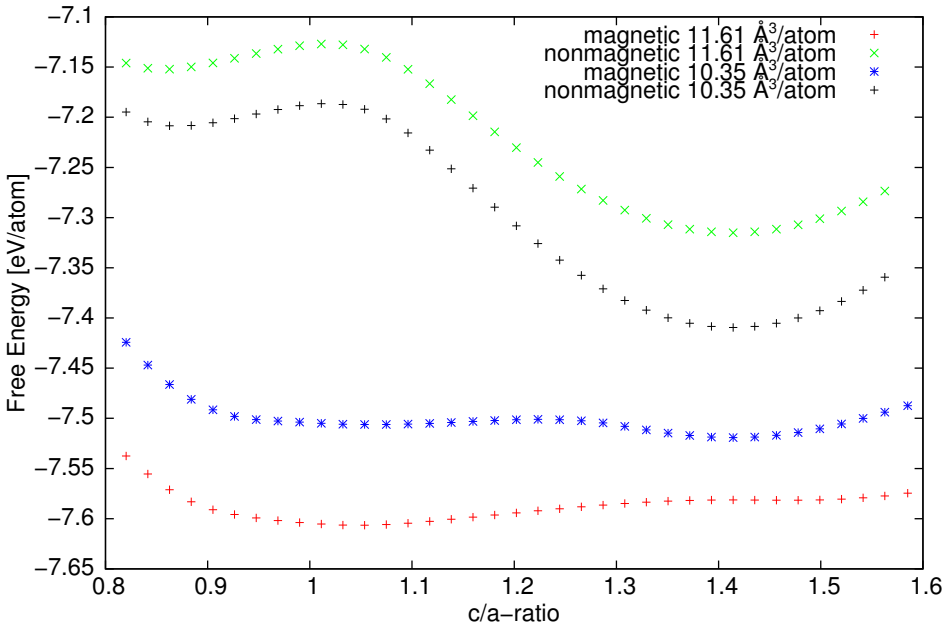

Figure 3.1: Free Energy of the magnetic and non-magnetic state as a function of the c/a-ratio for two different volumes.

$$\Delta E_{barr} = E_{max} - E_0, \qquad V = const. \tag{3.1}$$

The values for the energy barriers and the differences between the bcc-like and the fcc-like state are given in table 3.1.

	Ground State	ΔE_{barr} [eV/atom]	$\lvert\Delta E_{bcc-fcc}\rvert$ [eV/atom]
magnetic	bcc-like	0.0252	0.0250
non-magnetic	fcc-like	0.2230	0.2011

Table 3.1: Energy differences and barriers for different magnetic and structural configurations.

Comparing the magnetic and the non-magnetic state, an important difference is obvious: the energy barrier for a structural transformation is almost one order of magnitude higher for the non-magnetic state. In the non-magnetic case, the fcc-like state is the ground state for all volumes that are considered in the present work. Figure 3.1 shows that the energy barrier is lower for volumes larger than the equilibrium volume, but still its size makes a thermal excitation of the bcc-like state very improbable.

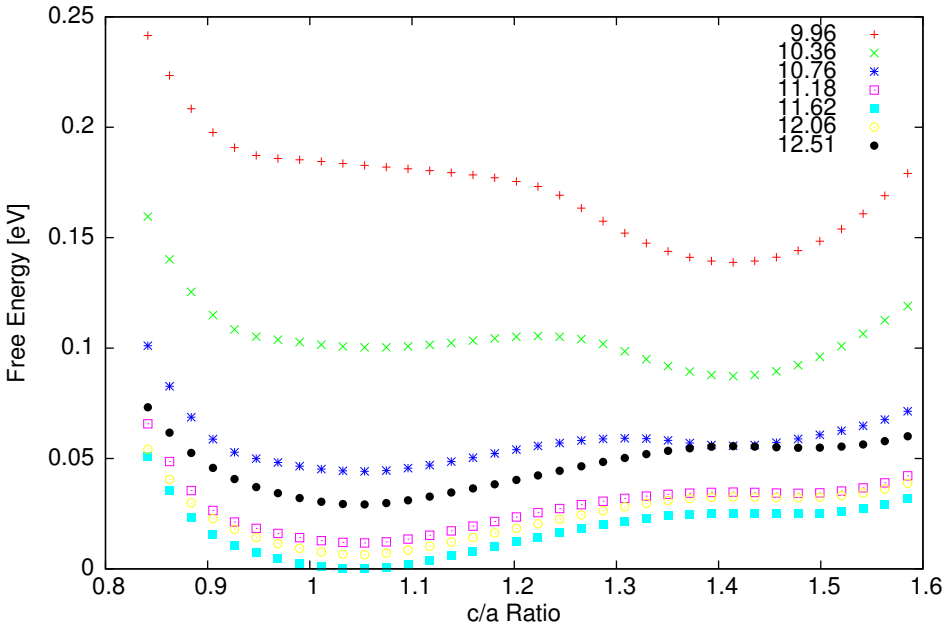

Figure 3.2: Free Energy of the magnetic state as a function of the c/a-ratio for seven different volumes [$Å^3$/atom]; the energy minimum is set to zero.

For magnetic Fe_3Ni, further computational results are visualized in figure 3.2, which shows the energy as a function of the c/a-ratio at different volumes across the range covered by the calculations. In order to ensure readability of the figure, only the data of seven different volumes are shown in the figure, although computations were performed for 21 volumes. The values in table 3.1 and the data in figure 3.2 show, that the energy barriers in the magnetic system are very low. In terms of thermal energy, the barrier at the equilibrium volume (25 meV) corresponds to a temperature of less than 300 K. Thus, at room temperature the probability of thermal excitation of the state is not negligible. On the other hand, the data in table 3.1 suggest that the local minimum is very shallow at equilibrium volume.

From figure 3.2 it is evident, that the bcc-like phase is not the ground state for small volumes. For both phases, the respective second minima are shallow over a wide range of volumes. In systems with very small volumes, the second minimum is even replaced by a saddle point. Hence, it is not probable that a thermally excited state can remain stable at any given volume. Therefore a phase transition from the bcc-like ground state to an fcc-like high temperature phase either needs a change in volume or additional effects, changing the shape of the energy surface.

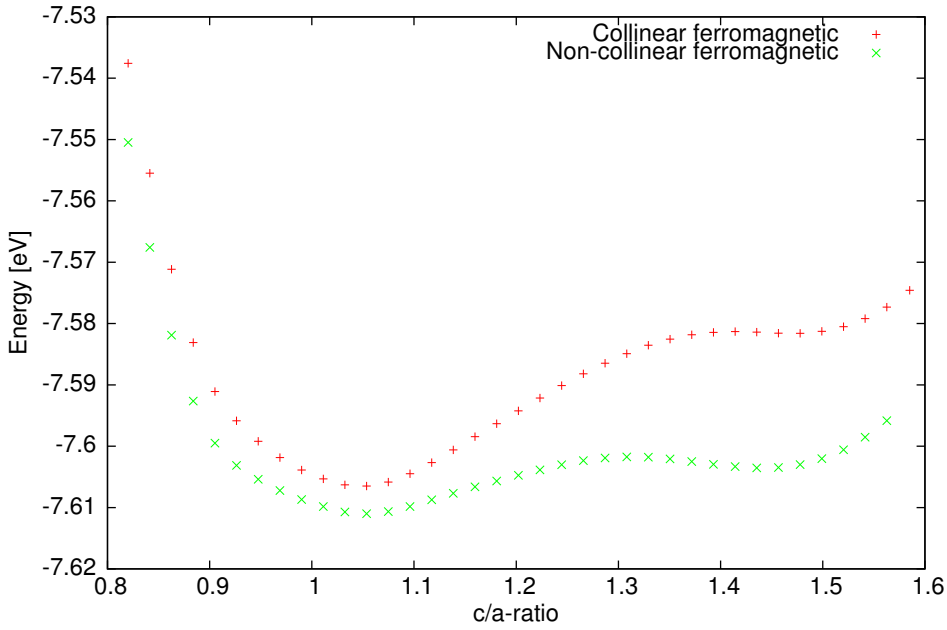

Figure 3.3: Comparison of Free Energy as a function of the c/a-ratio at equilibrium volume for collinear and non-collinear magnetism in Fe_3Ni.

Non-collinear magnetism Since in previous calculations (for example [27]) a non-collinear solution resulted in the lowest energy (see section 2.2.1), a non-collinear approach is also considered in the present diploma thesis. Indeed, the non-collinear state is found to have the lowest energy for all c/a-ratios and volumes, in accordance with the results described in section 2.2.1. The absolute values of the magnetic moments of the two magnetic approaches take very similar values. For example, in the energy minimum the magnetic moments are $|\mu^{coll}| = 8.577\ \mu_B$ and $|\mu^{noncoll}| = 8.567\ \mu_B$. A direct comparison of the two approaches is given in figure 3.3.

Both energy differences, $\Delta E_{barr} = 9.26$ meV and $\Delta E_{fcc-bcc} = 7.47$ meV, are significantly lower in the non-collinear than in the collinear magnetic state (for comparison, see table 3.1). Apart from the lower total energy and lower energy differences, the behaviour is very similar to that of the collinear state. At small volumes, the fcc-like phase is the ground state while in equilibrium and at large volumes the bcc-like phase has a lower energy.

However, there is a variety of non-collinear states leading to different energies and magnetic moments, which makes the task of finding the true ground state difficult. The major problem is that in some cases for different c/a-ratios with the same initial values for the components of the magnetic moment, different configurations are found to be the

ground state, leading to spikes of different energy in the energy surface. Furthermore no experimental evidence for non-collinear states has been found. Hence, the calculations in chapter 4 are based on the collinear results and for the Fe_5Ni_3 cell no non-collinear calculations have been performed.

3.1.2 Relaxation

From the analysis of the static calculations in the previous section, it is clear that the theoretical ground state of Fe_3Ni is the bcc-like phase. Since the static calculations only cover discrete points of volume and c/a-ratio, various calculations have been performed in order to determine the exact ground state. Furthermore it is interesting to analyse if the result of a relaxation depends on the starting point.
The relaxation has been performed using the so-called RMM-DIIS algorithm in VASP relaxing the cell shape and volume. This type of calculation is achieved by setting the tags IBRION=1 and ISIF=3. Different c/a-ratios at a volume of $V = 11.64$ Å^3/atom are used as starting points of the relaxation. Up to c/a-ratios of 1.25, the structure relaxes to the bcc-like form. In computations employing a different algorithm (the conjugate gradient algorithm, IBRION=2), even a starting value of $c/a = 1.35$ results in the bcc-like structure. Although the volume is allowed to change, it remains approximately constant during the relaxation process. This shows that the preferred structure is bcc-like at a volume of 11.64 Å^3/atom, which is very close to the equilibrium volume found in the static calculations.
In order to determine whether the bcc-like or the fcc-like state forms more likely from a mixed cell containing both structures, a corresponding supercell was constructed as a starting point of an ionic relaxation process. The supercell consists of 36 atoms building two fcc-like layers stacked onto two bcc-like layers on an fcc-like ground layer. Both fcc and bcc cell have a lattice constant of a=3.475, resulting in a small volume per atom for the fcc-like cell and a large one for the bcc-like cell. Since the total volume per atom is larger than the equilibrium volume found in the static calculations, change of the cell volume is enabled in the relaxation process. During the relaxation process the original cells are tilted and distorted and the volume shrinks significantly. Within the resulting structure, the formation of bcc-like cells of slightly different sizes is observed. The average volume per atom at the end of the relaxation 11.63 Å^3/atom. The original supercell and the result of the relaxation are depicted in figure 3.4. In the relaxed cell

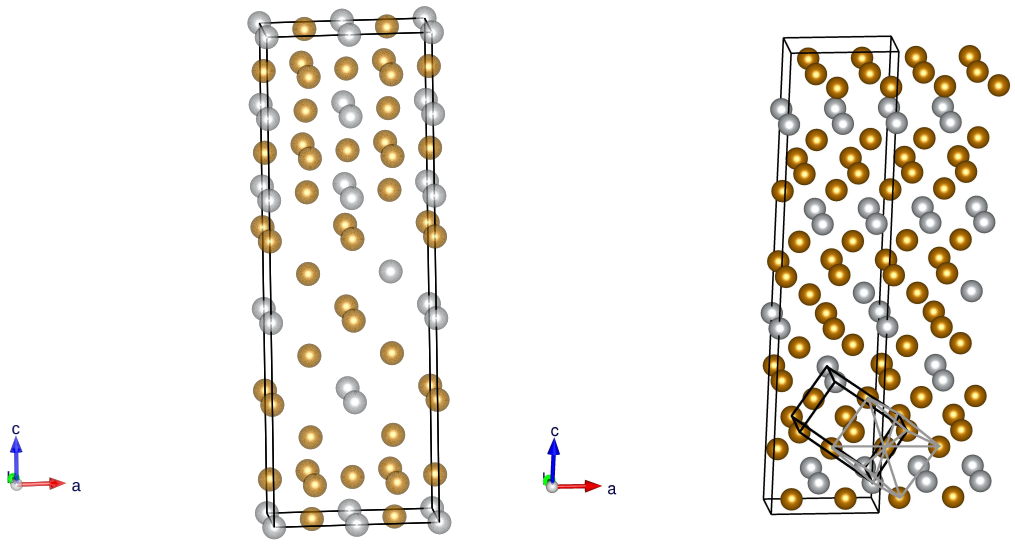

Figure 3.4: Fe_3Ni supercell in original (left) and relaxed (right) configuration. In the relaxed structure, a bcc-like cell is highlighted.

one of the bcc-like cells and the compressed fcc-like cell are marked with grey and black lines. It should be noted that the structures only approximately correspond to bcc-like cells because the distances between the atoms within the black cell deviate up to 5 % from each other. The reason for these deviations might be the presence of Ni-rich layers which probably do not occur in this form in the disordered crystal.
In the middle of the supercell there is a transition zone in fcc-like structure, followed by another bcc-like area. Probably the fcc-like part is metastable, because from the static calculations it is clear that the volume per atom is too large for an fcc-like ground state. The result of the relaxation can be interpreted as tendency of Fe_3Ni to form so-called tweed patterns, as they are found in other materials around the martensitic transformation [40].

3.2 Calculations of Fe_5Ni_3

3.2.1 Static Calculations

Except for the non-collinear magnetic system, the same calculations have been performed for Fe_5Ni_3. In contrast to the symmetrical Fe_3Ni cell, there are two possible Ni-places in the Fe_5Ni_3 cell presented in section 2.2.1. In addition to the structure illustrated in figure 2.4, where the third Ni-atom replaces the Fe-atom in the layer separating the two Fe_3Ni cells (xy-layer), there is a second not equivalent possible spot for the third Ni-atom in the cell. The other possibility is to replace one of the other two Fe-atoms in the side planes (xz or yz) of the Fe_3Ni cell. For both spots on the side planes this results in the same symmetry of the Fe_5Ni_3 cell.
In order to ensure that the existence of two possible configurations does not influence the behaviour of the model system, the calculations have been performed for both cells. For the non-magnetic state both configurations give approximately the same results. The fcc-like structure is the ground state and there is a second minimum for all volumes at $c/a \approx 0.85$. The shape of the $E(c/a)|_V$ curves is equivalent, only the energy values differ by up to one percent.
For the magnetic state the results are qualitatively similar; both configurations show a clear minimum at the fcc-like structure but the cell with the third Ni-atom in the centred position has a second shallow minimum near the bcc-like structure. In the alternative cell the minimum for the bcc-like structure does not exist. Since the bcc-like phase is the low temperature phase in the martensitic transformation, the existence of the minimum should not have an influence on the finite temperature calculations. The cell with the additional Ni-atom in the centred position is used for the following calculations, since it has higher symmetry than the other configuration.
Since the structure with two energetic minima was chosen for all the further considerations, it is also possible to compare the magnetic and the non-magnetic state. In contrast to Fe_3Ni the magnetic and the non-magnetic state both have their global energy minimum at the c/a ratio corresponding to the fcc-like structure. Over the whole volume range the magnetic state has a lower energy. As it is pointed out for Fe_3Ni, also for Fe_5Ni_3 the energy difference decreases at smaller volumes but the magnetic state is energetically more favourable at all the volumes and c/a-ratios covered in the present work.

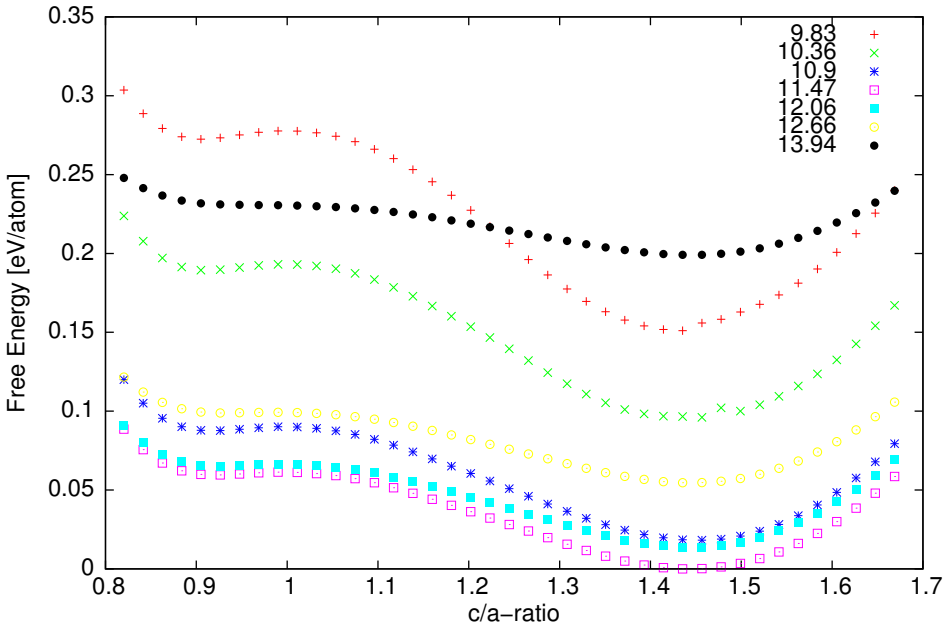

Figure 3.5: Free Energy of Fe_5Ni_3 for the magnetic state as a function of the c/a-ratio for seven different volumes [$Å^3$/atom].

In analogy to Fe_3Ni, the energy differences and barriers can be determined (see table 3.2).

	Ground State	ΔE_{barr} [eV/atom]	$\lvert\Delta E_{bcc-fcc}\rvert$ [eV/atom]
magnetic	fcc-like	0.0613	0.0596
non-magnetic	fcc-like	0.1849	0.1668

Table 3.2: Energy differences and barriers for different magnetic and structural configurations of Fe_5Ni_3.

For Fe_5Ni_3 there is essentially the same situation as for Fe_3Ni. In the non-magnetic case, the high energy barrier makes a transition impossible, while the barrier of the magnetic configuration is significantly smaller. However, the energy barrier of the magnetic state is approximately three times as high as in Fe_3Ni which decreases the transition probability significantly. Furthermore, the local minima near the bcc-like structure are very shallow; therefore the bcc-like state is not expected to be stable for any of the configurations considered in the present work. These facts are illustrated in figure 3.5, which depicts the free energy as a function of the c/a-ratio for seven different volumes including the equilibrium volume $V = 11.47$ $Å^3$/atom. Figure 3.5 shows that for small volumes the two-minima shape is more pronounced and the energy differences between the data

points are larger. One possible explanation for this behaviour is that for smaller lattice constants, the electrostatic configuration is more important, leading to pronounced minima for the structures with higher coordination numbers.

3.2.2 Relaxation

In order to find the equilibrium volume and to determine whether the fcc-like structure actually minimizes the energy, relaxations of the cell have also been performed for Fe_5Ni_3. Since the static calculations and the phase diagram in figure 2.5 indicate that Fe_5Ni_3 does not exist in the bcc-like structure, no relaxations concerning the starting point have been performed.
Starting from the fcc-like structure at $V = 11.47$ Å^3/atom, the cell volume, the cell shape and the ionic positions are allowed to change (IBRION=1, ISIF=3). The relaxed structure is face centered tetragonal with c/a=1.45, which is still considered an fcc-like structure. Furthermore, the cell volume increases slightly (V=11.495 Å^3/atom).
Another interesting property of the relaxed cell is that the Fe-atoms on the sites in the side planes shift towards the central layer (enriched in Ni) by approximately 1 % of the lattice constant. In order to investigate if this behaviour is the indicator for a larger reconstruction that is prevented by the periodic boundary conditions, the relaxation has also been performed for a larger supercell consisting of two Fe_5Ni_3 cells stacked on top of each other. However, the results of the relaxation of the supercell are equivalent to those of the single Fe_5Ni_3 cell; no additional deformations take place. This suggests that in Ni-rich areas, smaller cells could be preferred. Also the resulting c/a-ratio and equilibrium volume deviate only negligibly from the values of the relaxed single cell.

4 Finite temperature modelling

The calculations in chapter 3 provide information about the state of the system at $T = 0$ K. The aim of the present chapter is to introduce temperature to the model systems. There are different approaches to describe the temperature dependence of a system; in the present work, the finite temperature modelling is based on the phenomenological procedure described in section 2.3.1.

4.1 Energy Surfaces of the Model Systems in the Ground State

As a first step, an analytical expression of the energy surface of Fe_3Ni at $T = 0$ K has to be obtained. In the Landau expansion 2.23, this expression is given by a polynomial in the variables c/a and V. The lowest order polynomial that can reproduce the ab-initio data satisfactorily is found to be of the sixth order in c/a and of the third order in the volume. The resulting fit polynomial is given in equation 4.1.

$$E(c/a, V) = \sum_{i=0}^{6} \sum_{j=0}^{3} A_{ij} (c/a)^i V^j, \qquad \text{with} \tag{4.1}$$

$$A_{ij}^{\mathrm{Fe_3Ni}} = \begin{pmatrix} 5045.006695418 & -1509.59524336 & 148.38868092 & -4.78410872588 \\ -26151.23989000 & 7886.643555613 & -778.673032314 & 25.1686183179 \\ 55109.80832438 & -16772.2047598 & 1665.20504995 & -54.01086699 \\ -60312.7991148 & 18565.2780035 & -1856.67770442 & 60.5105148 \\ 36270.54477875 & -11315.0777834 & 1141.48482466 & -37.419536044 \\ -11415.4454152 & 3614.62336857 & -368.183814314 & 12.148020519 \\ 1476.17389989 & -474.79253419 & 48.8484051506 & -1.62250597774 \end{pmatrix}$$

(a)

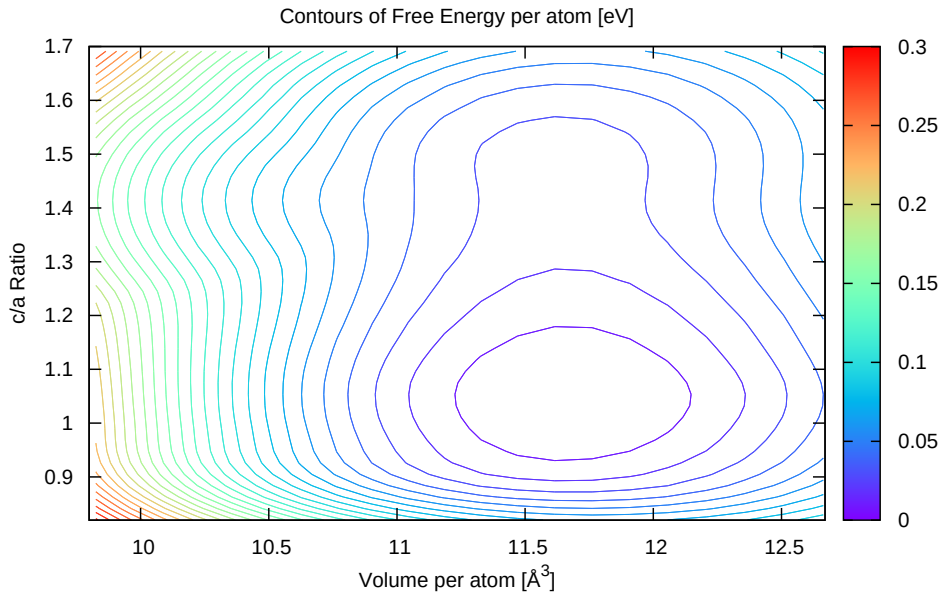

(b)

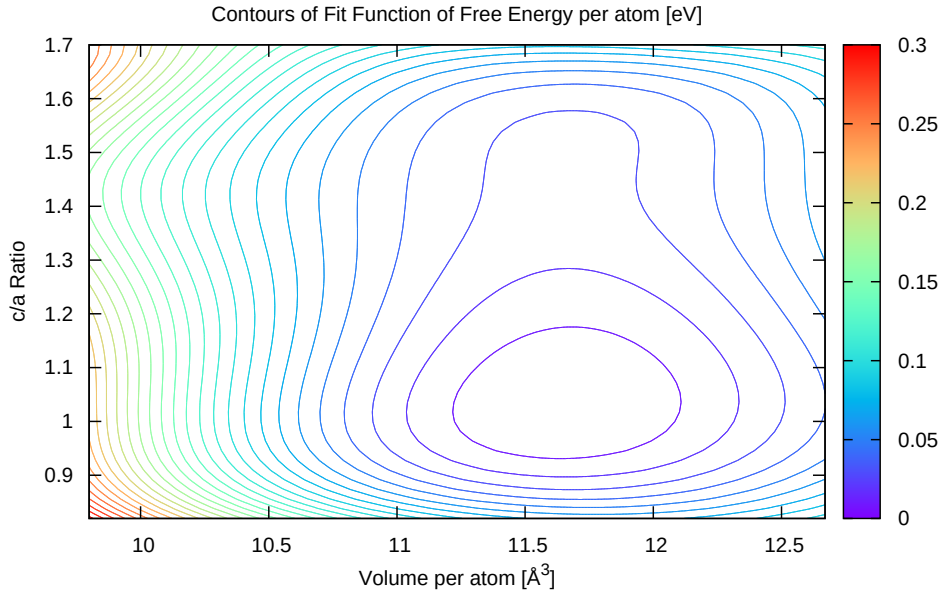

Figure 4.1: Comparison of the original data energy surface (a) and the fit (b) for Fe_3Ni

The high accuracy of the coefficients is necessary in order to reproduce the surface correctly. In figure 4.1 a comparison of the contours of the ab-initio data and the fit polynomial is given.
The fit reproduces the position and the form of the minima and the overall shape of the energy surface very well. There are small differences near $V = 11$ Å^3/atom, where the two structures have approximately the same energy, because the fit to a polynomial of sixth order in the c/a-ratio results in a shallower second minimum. The smoother shape of the fit is probably due to the discrete number of points of the computational data.
The contour graphics illustrate the small energy barrier between the two structures. Furthermore their bottle-like shape shows the fact that the lowest energy for both structures is approximately at the same volume.
For Fe_5Ni_3, the same fitting procedure is applied, leading to the coefficients

$$A_{ij}^{Fe_5Ni_3} = \begin{pmatrix} 1400.83114414 & -290.340117205 & 20.94791116214 & -0.516190932267 \\ -6535.44957548 & 1347.70484574 & -96.7737761327 & 2.373984215937 \\ 12153.9121867 & -2476.13989621 & 175.7810438133 & -4.264634854247 \\ -11239.54326548 & 2233.2493522857 & -154.8822909956 & 3.67452268616 \\ 5328.5168961 & -1006.5830761 & 66.420682571 & -1.498385574 \\ -1167.2667663 & 195.734104327 & -11.2386736986 & 0.21357489866 \\ 78.303304987 & -7.97035153871 & 0.065689359407 & 0.0094526300977 \end{pmatrix}.$$

The comparison of the data and the fit polynomial for Fe_5Ni_3 is depicted in figure 4.2. Again, the agreement of the position of the minima and the overall shape of the surface is very good and both minima occur approximately at the same volume. The small drop-shaped part of the contour connecting the two minima indicates the fact that the local minimum at this position is very shallow. The drop-like shape of the contour is less pronounced in the fit showing that the minimum is narrower in the fit.
The volume range covered in the calculations of Fe_5Ni_3 is larger than in those of Fe_3Ni, because in the finite temperature calculations irregularities of the fit at larger volumes influenced the results before additional values were included.

(a)

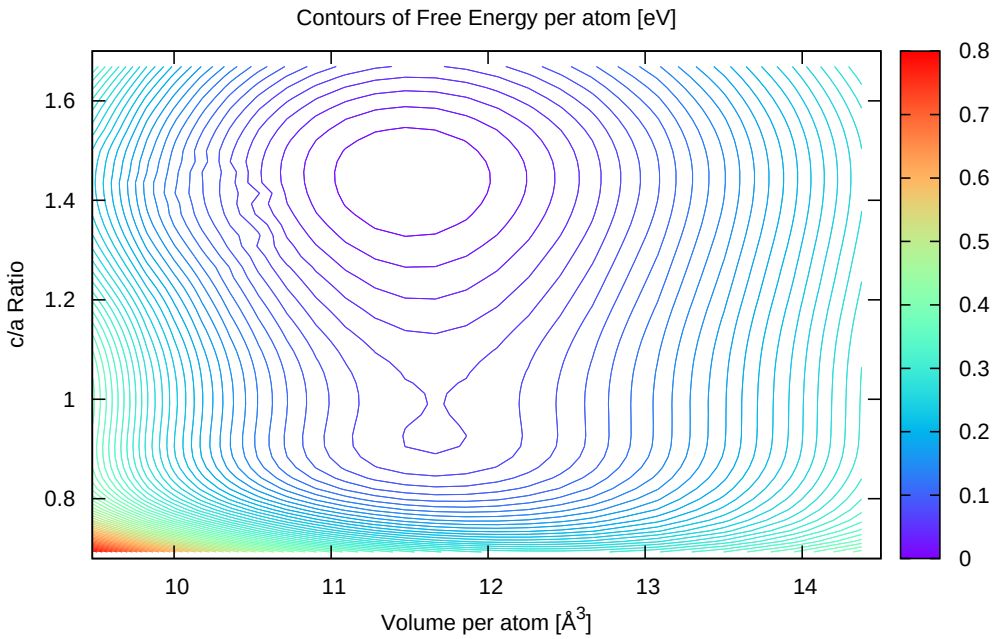

(b)

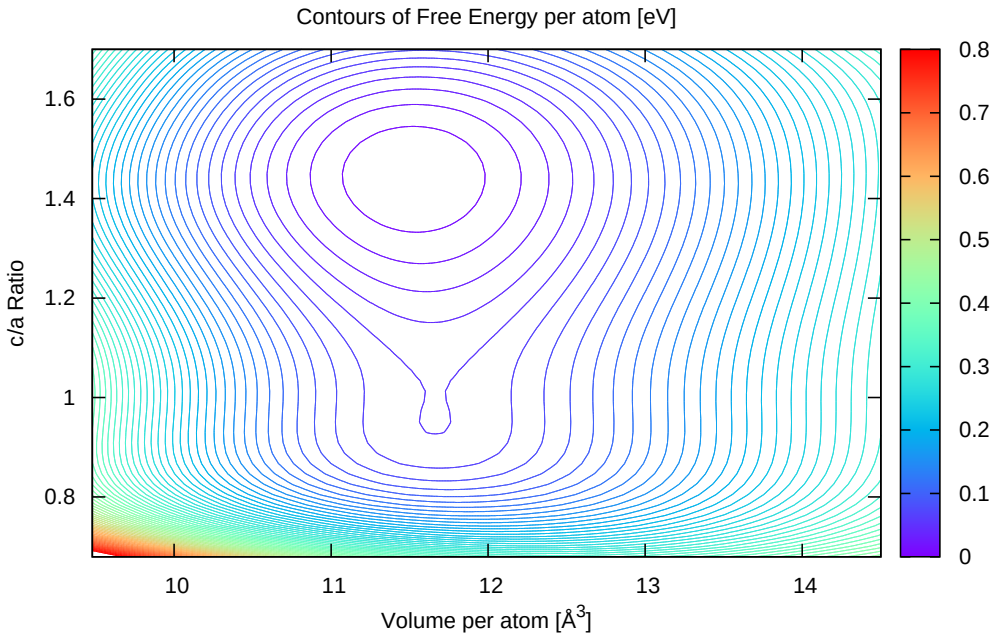

Figure 4.2: Comparison of the original data energy surface (a) and the fit (b) for Fe_5Ni_3

4.2 Interpolation of Energy Surfaces between the Model System Concentrations

Since the two model systems considered in the present work correspond to concentrations below and above the original Invar composition ($Fe_{65}Ni_{35}$), it is possible to interpolate between the two structures. An interpolation allows the investigation of the finite temperature properties of systems with different compositions. Furthermore the concentration dependence of the system's characteristics and the concentration, at which the fcc-like and the bcc-like structure have the same energy, can be determined.
The two model systems presented in chapter 3 are the only two sampling points of the concentration dependent energy surface. Hence, a linear concentration dependence of the fit coefficients is assumed. The coefficients at a given concentration C_{Ni} are calculated using the expression given by equation 4.2.

$$\begin{aligned} A_{ij}(C_{\mathrm{Ni}}) &= \frac{A_{ij}(C_{\mathrm{Ni}}=0.375)-A_{ij}(C_{\mathrm{Ni}}=0.25)}{0.125} \cdot C_{\mathrm{Ni}} + \\ &\quad + \Big(A_{ij}(C_{\mathrm{Ni}}=0.25) - \frac{A_{ij}(C_{\mathrm{Ni}}=0.375)-A_{ij}(C_{\mathrm{Ni}}=0.25)}{0.125} \cdot 0.25\Big) \end{aligned} \tag{4.2}$$

Figure 4.3 illustrates the concentration dependence of the shape of the energy surface, the position of the minima and the energy barrier. The results of the interpolation show that at a Ni-concentration between 29 % and 30 % the two minima have the same energy and the energy barrier is very low. At this composition, the two structures are in equilibrium. This result is in good agreement with the phase diagram in figure 2.5, in which the coexistence of an fcc-like phase begins at a minimum Ni-content of approximately 30 %. With increasing Ni content, the energy minimum of the fcc-like structure stabilizes, since the energy barrier increases and the minimum of the bcc-like structure becomes shallow and increases in energy.

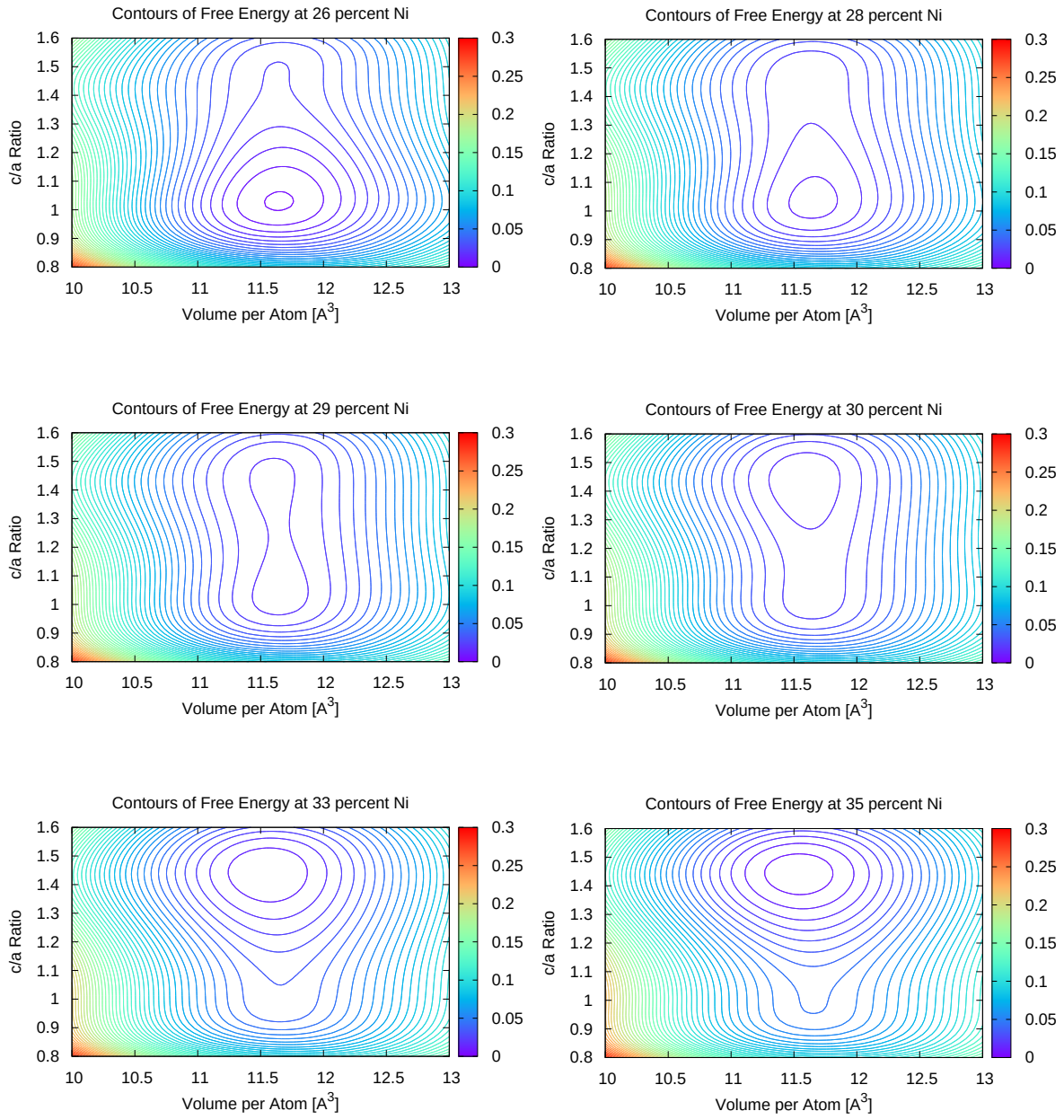

Figure 4.3: Interpolated free energy contour plots for six different Ni concentrations: $Fe_{74}Ni_{26}$, $Fe_{72}Ni_{28}$, $Fe_{71}Ni_{29}$, $Fe_{70}Ni_{30}$, $Fe_{67}Ni_{33}$ and $Fe_{65}Ni_{35}$. The fcc-like phase is the ground state for $C_{\mathrm{Ni}} \geq 30$ %.

4.3 Self-consistent Solution of the Equations of State

In order to investigate the temperature dependence of the system, the equations of state of the system including the fluctuations (equations 2.29, 2.30) have to be solved self-consistently to determine the equilibrium value of the fluctuations.
The thermal dependence of the volume and c/a-ratio fluctuations is controlled by two quantities: the cut-off k-vectors (k_c and q_c) and the stiffness constants (K and Q). The stiffness constants determine the width of the k-space distribution of the fluctuations. These values are not directly accessible in the experiment, but they can be related to the correlation lengths of the fluctuations, which can be determined in neutron scattering experiments. Unfortunately no experiments determining the correlation lengths of the volume and c/a-ratio fluctuations of Fe_3Ni could be found in the literature; therefore the stiffness constants and the cut-off k-vectors are treated as adjustable parameters. This is possible, because the physical information is for the most part contained in the energy surfaces whereas the parameters basically only influence the temperature scale of the phase transition.
The parameters are adjusted in order to yield physically meaningful values of the fluctuations and a transition temperature of Fe_3Ni in the martensitic transition region in figure 2.5. The values used for the parameters in the present work are listed in table 4.1.

K	16	eV Å^2
Q	$7{\cdot}10^{-3}$	eV/Å^4
k_c	5.2	Å^{-1}
q_c	6.4	Å^{-1}

Table 4.1: Values of the parameters determining the fluctuations of the system.

Since the self-consistent solution of the equations can only be calculated numerically, a Fortran program was written for this task. The structure of the program is presented in the following section.

4.3.1 Numerical Solution of the Self-consistent Equations

The Fortran program solves the self-consistent equations for a given set of temperatures. For each temperature a "do while"-loop is used to minimize the four expressions

$$\begin{array}{rcll} \frac{\partial E}{\partial V} + \frac{\partial \phi}{\partial V} + P & = & \Delta_{11}, & c/a = const, \\ \frac{\partial E}{\partial (c/a)} + \frac{\partial \phi}{\partial (c/a)} & = & \Delta_{12}, & V = const, \\ |\langle \xi^2 \rangle_n - \langle \xi^2 \rangle_{n+1}| & = & \Delta_{21}, & \\ |\langle \nu^2 \rangle_n - \langle \xi^2 \rangle_{n+1}| & = & \Delta_{22}, & \end{array} \tag{4.3}$$

in which P represents the external pressure, which is set to $7 \cdot 10^{-7}$ eV/Å^3 $\approx$ 1 bar. However, it should be noted that pressures of this order of magnitude have no influence on the calculation. First, the values of V and c/a are adapted stepwise using Newton's method (see equation 4.4).

$$\begin{array}{rcl} V_{n+1} & = & V_n - \Delta_{11} \left(\frac{\partial \Delta_{11}}{\partial V} \right)^{-1} \\ (\frac{c}{a})_{n+1} & = & (\frac{c}{a})_n - \Delta_{12} \left(\frac{\partial \Delta_{12}}{\partial (c/a)} \right)^{-1} \end{array} \tag{4.4}$$

The analytic expressions for Δ_{11}, Δ_{12}, $\frac{\partial \Delta_{12}}{\partial (c/a)}$, $\frac{\partial \Delta_{11}}{\partial (V)}$ are implemented as subroutines. With the new values for the volume and c/a-ratio, equations 2.29 are used to calculate the corresponding values of the fluctuation amplitudes for the given temperature. The different fluctuation amplitudes change ϕ, the energy contribution of the fluctuations. In the following run of the loop, ϕ is used to determine the new values of V and c/a. This process is repeated until the values Δ_{ij} with $i, j = 1, 2$ reach zero with a predetermined accuracy; in the present program $\Delta_{max} = 10^{-7}$ terminates the loop. In order to prevent infinite loops, the loop stops after 10^5 runs, returns a message and restarts with different initial values. As soon as a result is found, the program verifies if it is within the fit range including its surroundings, which are set to 8 Å^3 to 16 Å^3 for the volume and 0.8 to 1.7 for the c/a-ratio. If the result is outside this range, it is assumed to be caused by a numeric instability, for example a small value of the derivatives in equations 4.4, and the calculations are restarted from different initial values.
A solution meeting the criteria mentioned above is assumed to be an equilibrium state for the given temperature. Hence the fluctuation amplitudes determined by the program

describe the thermal evolution of the system and they can be used to calculate the physical ground state given by the minimum of the total energy U.
The minimization of U also uses Newton's method and is implemented similarly to the calculation of the solution of the equations of state, but with the important difference that the fluctuation amplitudes are constants. Thus, only the volumes and c/a-ratios are varied to find the minimum. Since Newton's method is sensitive with respect to the initial position, the search for the minimum of U is performed twice, once starting from $c/a = 1$ (bcc-like) and once starting from $c/a = 1.4$ (near fcc-like). The energies of the two results are compared and the lower one is assumed to be the ground state. Once the minimum of U is obtained, many properties of the system can be calculated. In the program, the difference in entropy (given by equation 2.31) compared to the entropy of first temperature in the calculation, the bulk modulus

$$B = V \frac{\partial^2 U}{\partial V^2}, \tag{4.5}$$

the thermal expansion coefficient and the elastic constant of tetragonal deformation

$$C' = \frac{1}{V} \frac{\partial^2 U}{\partial (c/a)^2} \tag{4.6}$$

are calculated. The thermal expansion coefficient for the first temperature in the loop is set to zero; for the other temperatures it is given by

$$\alpha = \frac{1}{3V} \frac{\Delta V}{\Delta T}. \tag{4.7}$$

After finishing the loop over the temperatures, these characteristics of the system are plotted as a function of temperature, giving the thermal evolution of the system. Furthermore, for each temperature, a contour plot of the total energy in the surroundings of the minimum is produced. As a first test of the validity of the results, one can check whether at $T = 0$ K the total energy surface is equivalent to the free energy surface obtained in the ab-initio calculations. Since at $T = 0$ K there are no contributions of fluctuation terms, the energy surface must not change compared to the results of the static calculations.

4.4 Results of the Finite Temperature Model

The finite temperature modelling has been performed for eight different compositions of the Fe-Ni alloy and at various temperatures. Therefore only selected results are presented in the present work.
The most interesting process in the finite temperature calculations is the phase transition between the bcc-like and the fcc-like state since it influences the thermal expansion and the elastic constants of the system and it is concentration dependent. The concentration dependence establishes a connection to experiments and can hence be regarded as an indicator of the quality of the modelling process. A good model should reproduce experimental data such as the phase diagram in figure 2.5 correctly.
In the present chapter, first the temperature evolution of the Fe_3Ni system is presented. Then a comparison is drawn to the behaviour of systems with different Fe and Ni contents. The absolute values of the temperatures are not very informative since they can be adjusted by changing the parameters k_c and K; q_c and Q have less influence. Therefore all temperatures are given in units of the transition temperature T_M of Fe_3Ni.

4.4.1 Temperature Evolution of Fe_3Ni

In Fe_3Ni the volume fluctuations are found to cause a distortion of the energy surface. In figure 4.4, the total energy surfaces for six different temperatures in a temperature range around the transition temperature are depicted. In the total energy graphics, the terms $\frac{k_B T}{2} \sum_{k \leq q_c, k_c}$ in equation 2.32 are neglected, since they correspond to the number of modes and thus only contribute a constant value for a given temperature.
The first contour plot in figure 4.4 shows that the energy surface remains essentially unchanged for low temperatures. Hence, one graphic is sufficient to show the changes in the energy surface below half the transition temperature. With increasing temperature the minimum at the bcc-like structure drifts towards larger volumes, as one would expect from thermal expansion. The second minimum at the fcc-like structure, however, shifts to smaller volumes. From the comparison of the first two contour plots in figure 4.4 one can infer that the energy barrier between the two states decreases until the temperature reaches half the transition temperature. At higher temperatures the energy barrier remains approximately constant but the energy difference decreases until at $T = T_\mathrm{M}$ the

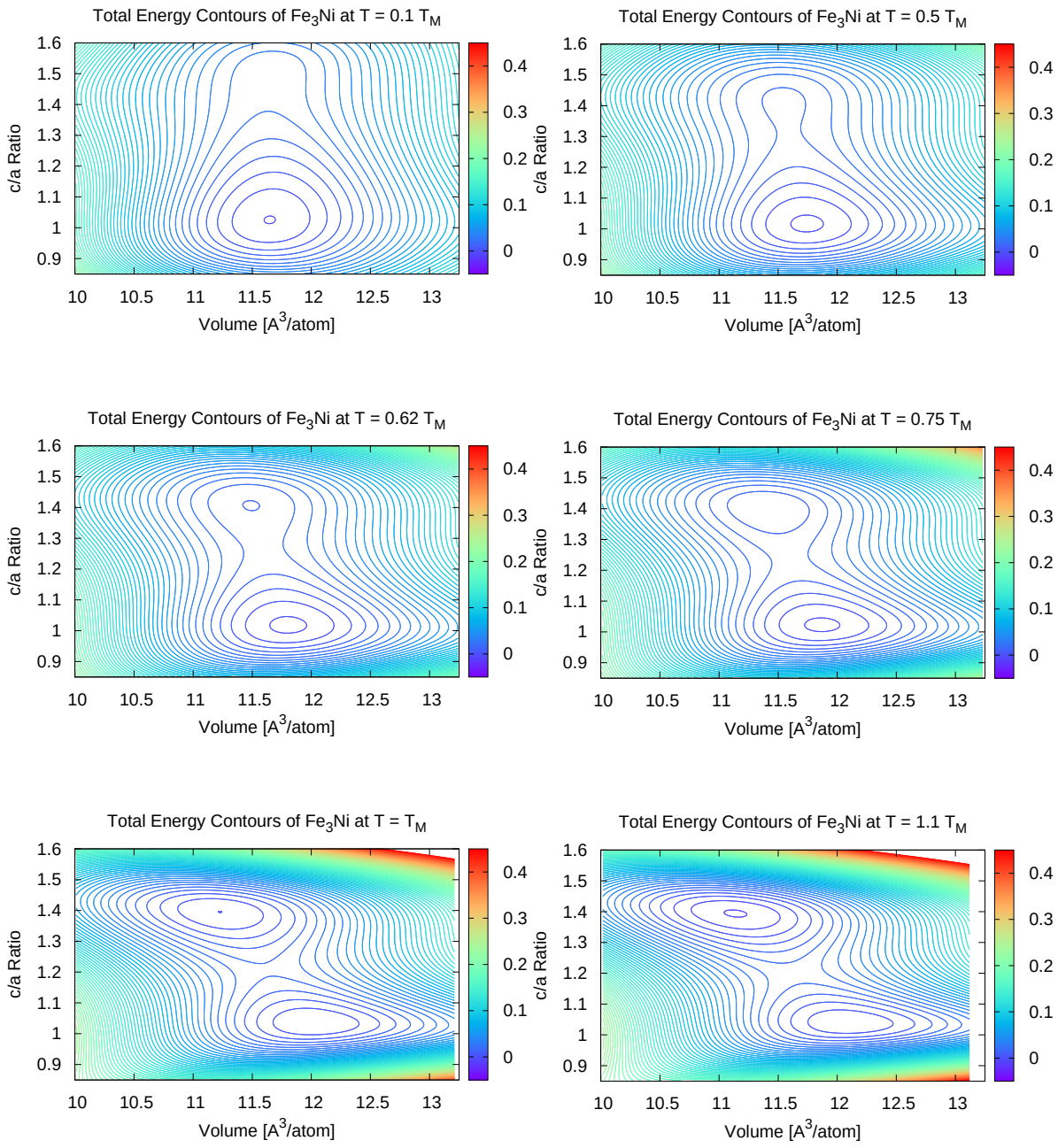

Figure 4.4: Energy surfaces for Fe_3Ni for six different temperatures. With increasing temperature, the minimum at the fcc-like structure stabilizes and shifts towards smaller volumes.

fcc-like structure becomes the ground state. A further increase in temperature causes the volume of the stable minimum to decrease and the energy barrier between the states to increase.

From the shape of the energy surfaces, one can already infer how the elastic constants and the thermal expansion coefficient depend on the temperature. Up to the transition temperature the fluctuations cause the volume to increase, leading to a positive thermal expansion. The minimum corresponding to the fcc-like state, however, is shifted towards smaller volumes with increasing fluctuation amplitude. This unexpected behaviour is already implied in the shape of the energy surface at $T = 0$ K. In order to illustrate this fact figure 4.5 shows the volume dependence of the energy for the fcc-like and the bcc-like structure. For the fcc-like structure, the energy costs of a contraction are smaller than those of an expansion of the lattice. Thus, if thermal expansion is interpreted as the shift of the mean volume to larger values at higher energies, the fcc-like structure is expected to show negative thermal expansion owing to the volume dependence of the energy. In contrast, the energy curve of the bcc-like structure is steeper at volumes smaller than the minimum and flatter at larger volumes, corresponding to the ordinary case of a positive thermal expansion coefficient.

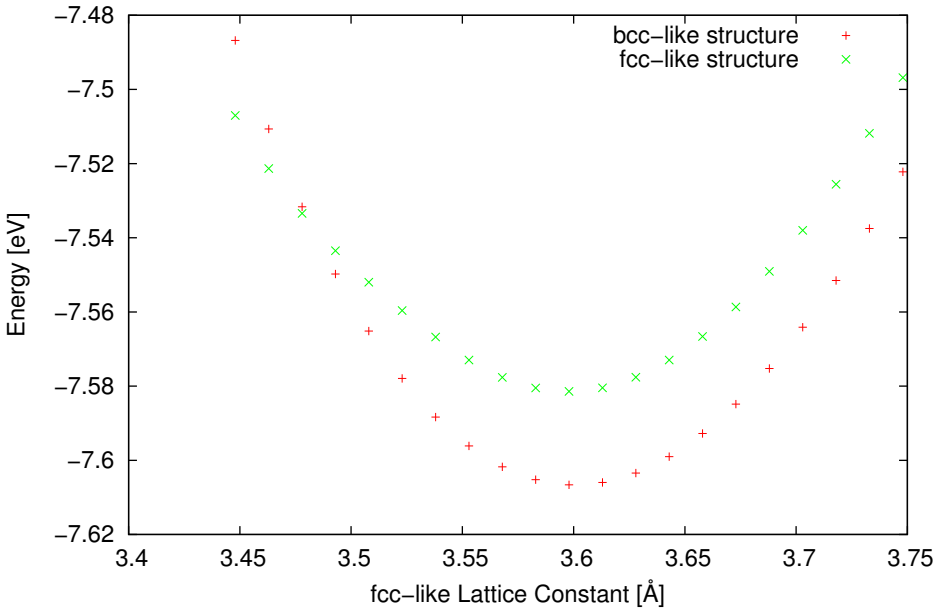

Figure 4.5: Energy as a function of the fcc-like lattice constant for the fcc-like and bcc-like structure, showing that the shape of the energy curve of the fcc-like structure favours negative thermal expansion

The finite temperature calculation confirms the assumption based on the shape of the energy surface at $T = 0$ K. Figure 4.6 shows the results for the temperature dependence of the volume and the thermal expansion coefficient. As predicted, the system expands with increasing temperature while its structure is bcc-like. At the transition temperature, the system changes to the fcc-like structure, which takes approximately the same volume as the bcc-like structure at $T = 0$ K but shifts towards smaller volumes with increasing temperature. Hence at the transition temperature a discontinuity in the volume occurs, leading to an undefined value of the thermal expansion coefficient. Numerically, α has a large negative value at this temperature, which is not included in figure 4.6. Neglecting this point is justified because its value depends on the step size of the temperature loop; thus it has no physical significance. At temperatures $T > T_{\mathrm{M}}$ the thermal expansion coefficient takes negative values in agreement with the shape of the energy surface discussed above. Since the martensitic transition occurs gradually in the bulk and is found near the Invar region (see figure 2.5), this effect certainly contributes to the Invar behaviour. However, the fact that α decreases even further from relatively large negative values indicates that for $T >> T_{\mathrm{M}}$ the reduction of the structural considerations to only two fluctuating variables (the volume and the c/a-ratio) is not a good approximation any more.
Since the magnetic effects, which are the basis of the Invar effect according to the theories discussed in chapter 2.2.1, are not considered, the positive thermal expansion coefficient in the bcc-like structure should not be interpreted as failure of the theory to reproduce Invar behaviour. Instead, the positive thermal expansion coefficient represents the case of constant magnetic moments. Hence, it can be interpreted as a further verification that the Invar effect below the temperature of the martensitic transformation is based on magnetism.
An overview of the temperature dependent properties of the system is given in the figures 4.6, 4.7 and 4.8. The mean square values of the fluctuations are not illustrated in any figure since they simply increase linearly with temperature in a good approximation over the whole temperature range. At the transition temperature they take the critical values $\langle \nu^2 \rangle_c \approx 14$ Å^6 and $\langle \xi^2 \rangle_c \approx 0.009$. The fluctuations of the volume are very large; the root mean square value corresponds to fluctuations of the lattice constant of approximately ten percent. One possible reason why the transition only occurs at these high critical fluctuations is that the magnetovolume effects, which could lead to smaller volumes favouring the fcc-like state, are neglected completely.

Figure 4.7 illustrates the temperature dependence of the c/a-ratio and the entropy

(a)

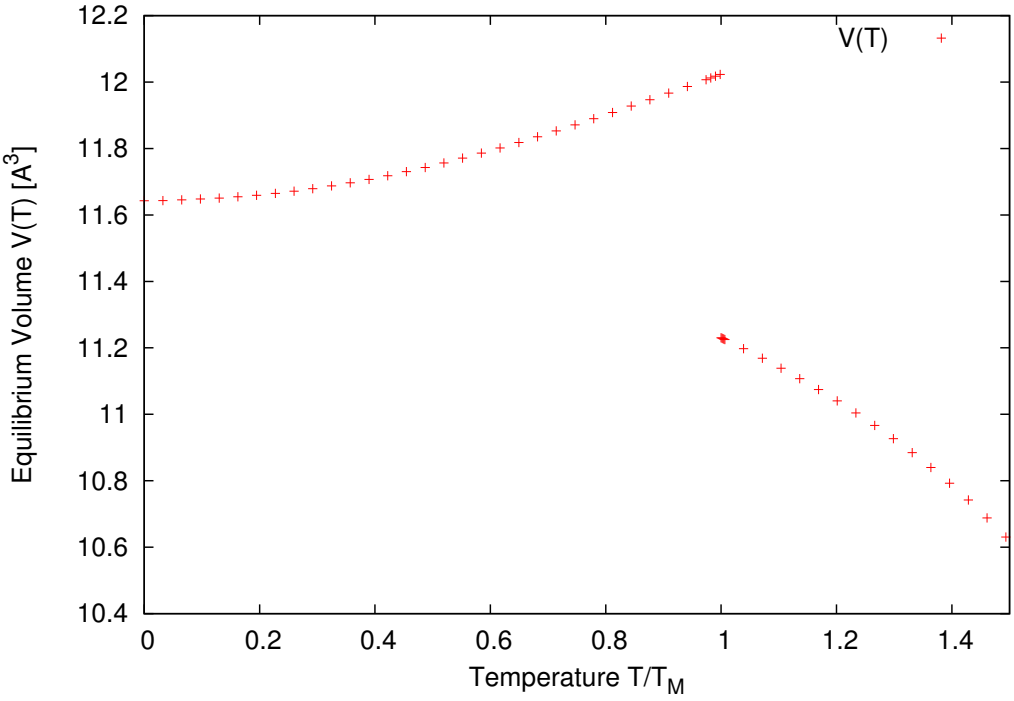

(b)

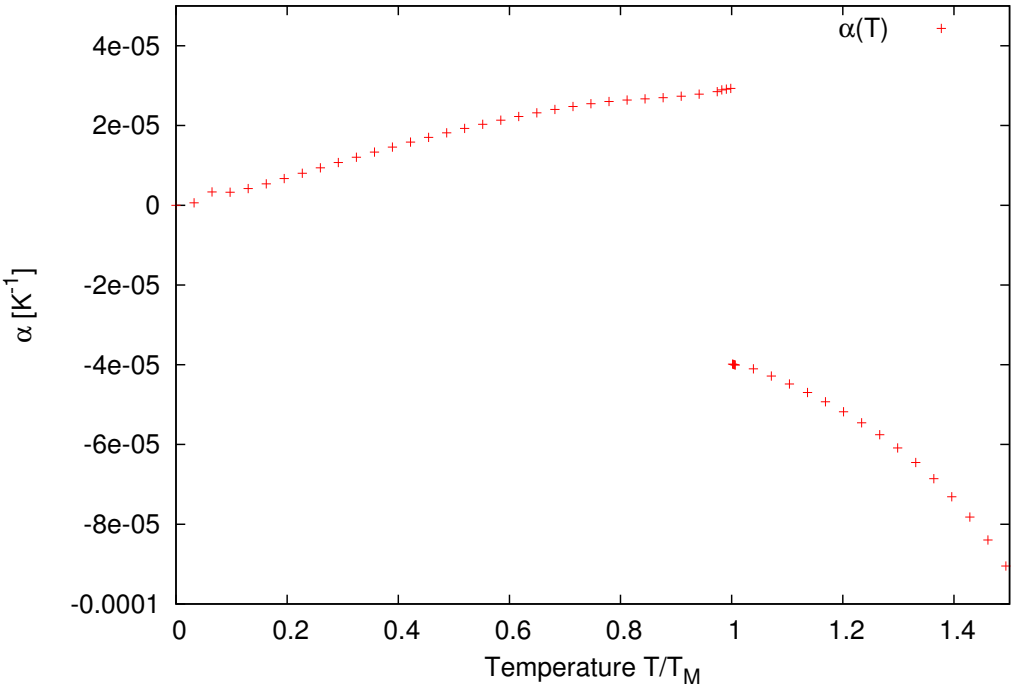

Figure 4.6: Temperature dependence of the volume (a) and the thermal expansion coefficient α (b) of Fe_3Ni. Both variables show that the thermal expansion is positive in the bcc-like phase negative in the fcc-like phase.

(a)

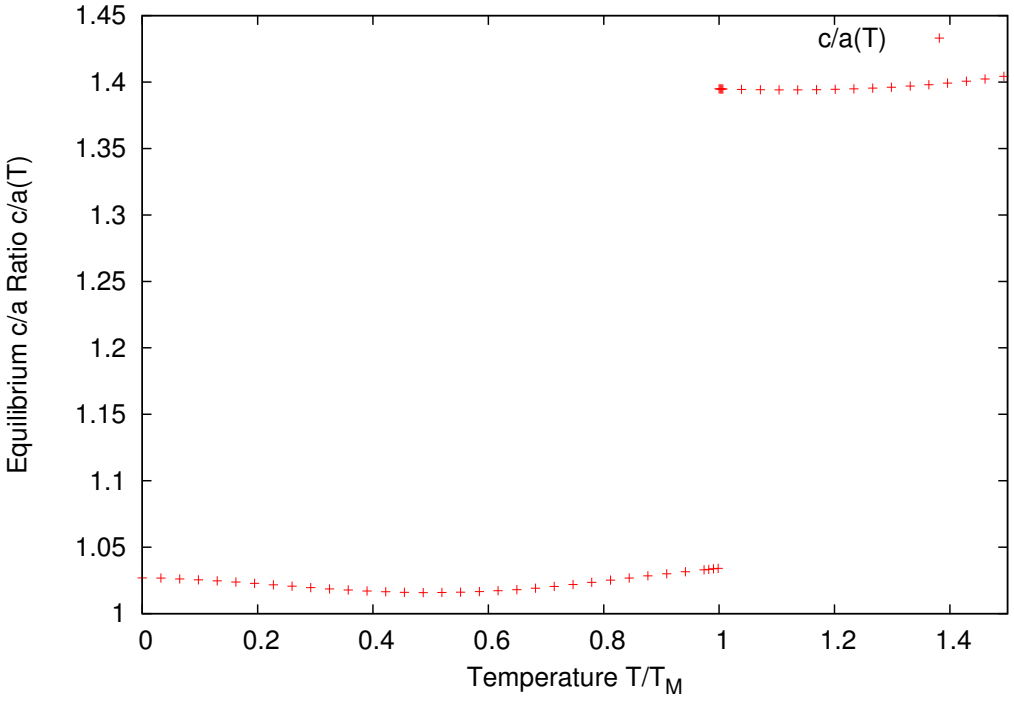

(b)

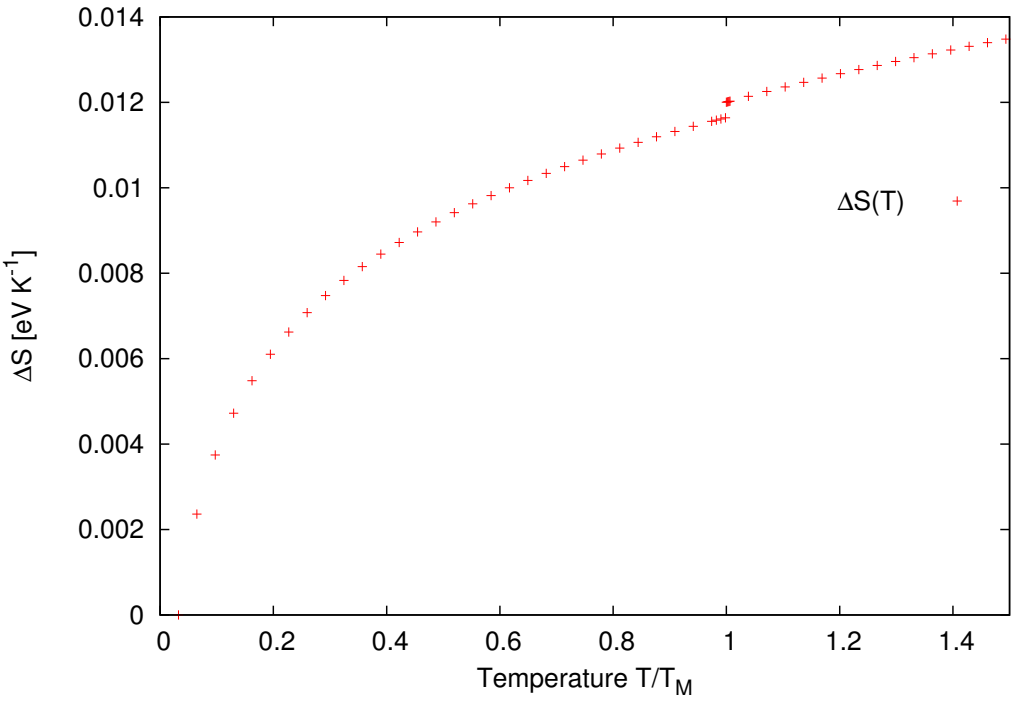

Figure 4.7: Temperature dependence of the c/a-ratio (a) and the entropy difference to $T = 0$ K (b) of Fe_3Ni. Both quantities clearly show the phase transition at $T = T_M$. The behaviour of ΔS is typical for entropy driven phase transitions.

(a)

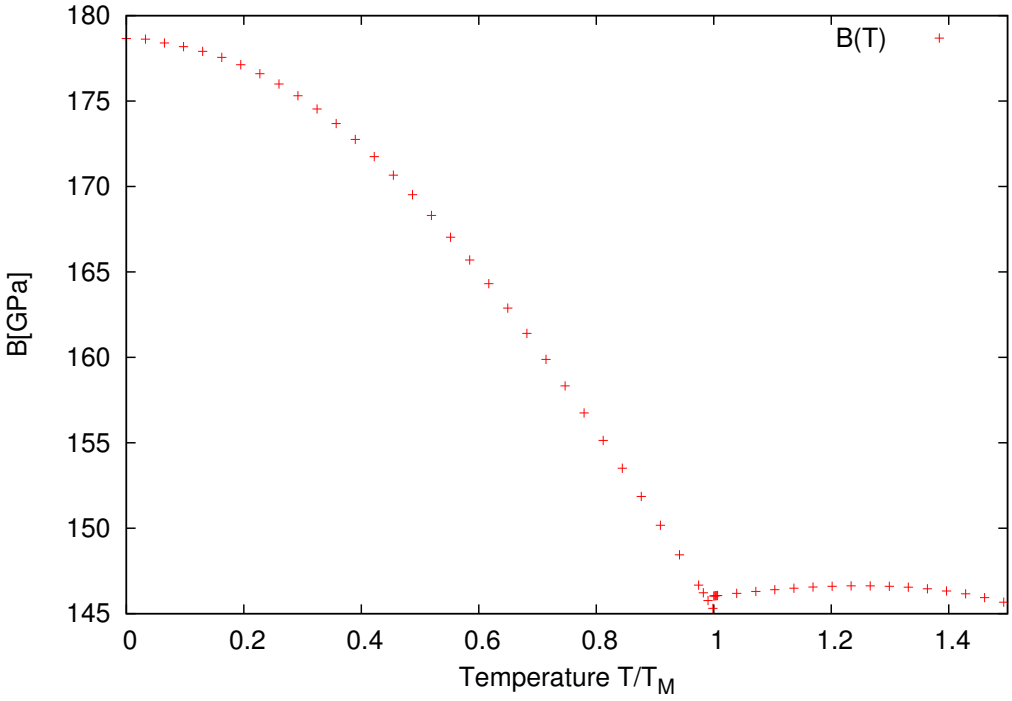

(b)

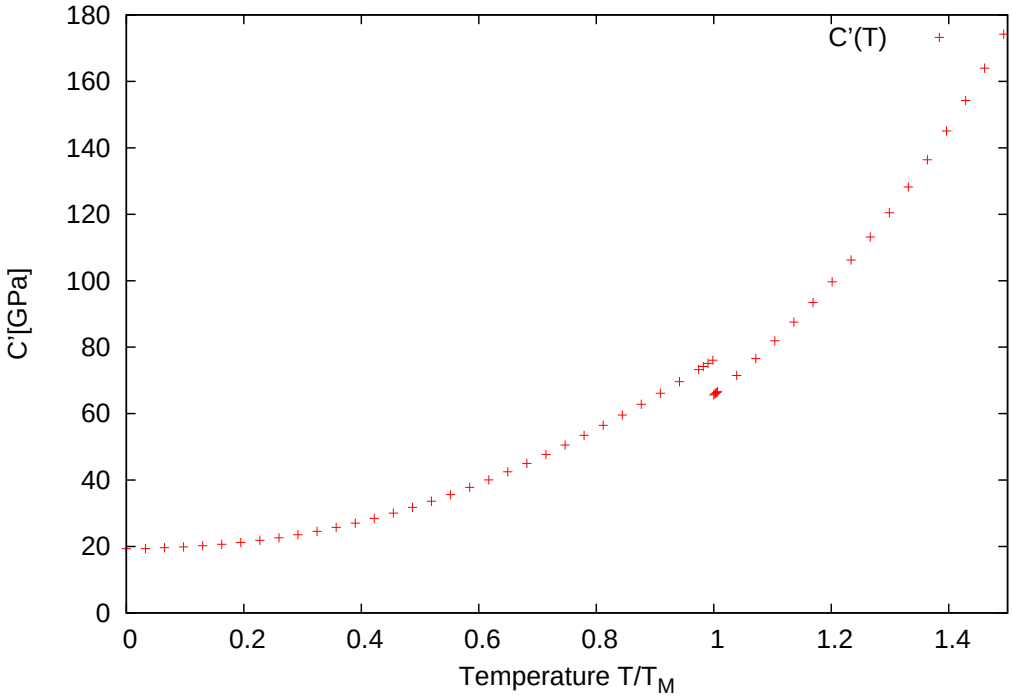

Figure 4.8: Temperature dependence of the bulk modulus B (a) and the elastic constant C' (b) of Fe_3Ni. After the discontinuity corresponding to the phase transition, the bulk modulus remains nearly constant whereas the behaviour of C' is similar for both states.

difference compared to $T = 0$ K. The c/a-ratio shows the transition from the bcc-like to the fcc-like state. The variation of the c/a-ratio before and after the transition is caused by small changes of the energy surface owing to the fluctuations.
The entropy rises with temperature since the fluctuation amplitudes, which represent thermal disorder, increase with temperature. The discontinuity in the entropy is typical for entropy driven phase transitions [41]. Since the total energy is a continuous function of the temperature, the step to a higher entropy corresponds to negative step in the free energy, resulting in an energy difference favouring the phase transition.
The thermal dependence of the elastic constants is illustrated in figure 4.8. In the experiments cited in the review by Shiga [13] the elastic constants for $Fe_{65}Ni_{35}$ take the values $B = 106$ GPa and $C' = 22$ GPa at room temperature. The comparison to the model for Fe_3Ni shows that for both parameters the values cannot be reproduced correctly, although the bulk modulus shows a tendency towards lower values for higher temperatures. C' is close to the experimental value at low temperatures but the deformation of the energy surface caused by the volume fluctuations leads to a strong increase. Since C' is proportional to the second derivative of the energy with respect to the c/a-ratio at constant volume, it is clear that it increases as soon as the positions of the minima shift to different volumes. In order to explain the discrepancy compared to the experiment, it is important to note that a full description of the elastic behaviour of the system cannot be given by only two elastic constants. It is possible that including shear strain into the calculations could lead to a more accurate description of the system's elastic behaviour. Concerning C', it is possible that its enormous increase with temperature is caused by reducing the description of the system to two structural degrees of freedom. However, including a third variable would also increase the complexity of the calculation significantly. Another fact which must not be neglected in the analysis of the results is that the finite temperature modelling does not consider changes in the magnetic moment, which also have influence on the elastic properties.
Finally, it should be noted that the transition to the fcc-like phase can also be induced by external pressure. The critical pressure for this transition at $T = 0$ K is approximately $P_c = 16.4$ GPa, which is comparable to the critical pressure found in similar calculations for Ca by Mohn et al. [33].

4.4.2 Temperature Evolution of Model Systems with Different Compositions

In the present section, the results for Fe_3Ni at finite temperature are compared to a selection of the model systems presented in section 4.2: $Fe_{71}Ni_{29}$, $Fe_{69}Ni_{31}$ and $Fe_{65}Ni_{35}$. On the examples of $Fe_{71}Ni_{29}$ and $Fe_{69}Ni_{31}$ it can be shown that with increasing Ni-content the transition temperature decreases. At concentrations $C_{\mathrm{Ni}} \geq 30$ %, the system's ground state is already the fcc-like structure (see figure 4.3). Thus, based on the phase diagram (figure 2.5), no transition is expected for these concentrations. Indeed the finite temperature model shows no transition but a further stabilization of the fcc-like structure at increasing temperatures. Although no transition occurs either, $Fe_{65}Ni_{35}$ is included in the comparison, because it is the original Invar composition found by Guillaume [1]. In order to ensure a meaningful comparison, the same values of the parameters K, Q, k_c and q_c are used over the whole concentration range. Furthermore, the temperature scale is given in units of the transition temperature T_{M} of Fe_3Ni.

First, the properties of the materials near the critical composition are compared. Figure 4.9 shows a comparison of the temperature dependence of the equilibrium volume of $Fe_{71}Ni_{29}$ and $Fe_{69}Ni_{31}$. Clearly, the phase transition in $Fe_{71}Ni_{29}$ occurs at a significantly lower temperature ($<0.2T_{\mathrm{M}}$) than in Fe_3Ni. The lower transition temperature means that smaller fluctuations are needed to initiate the phase transition. In this case, the critical fluctuation amplitudes are $\langle\nu^2\rangle_c \approx 2.5$ Å^6 and $\langle\xi^2\rangle_c \approx 0.0016$. Furthermore, figure 4.9 illustrates that no structural phase transition occurs for $C_{\mathrm{Ni}} = 31$ %. Similarly to the considerations concerning Fe_3Ni, negative thermal expansion is found in the fcc-like phase for both Ni-concentrations. The temperature loop for other compositions than Fe_3Ni only includes temperatures up to $T \approx 0.75 \cdot T_{\mathrm{M}}$ since it is clear from the total energy surfaces in figure 4.10 that the fcc-like minimum is stable and no transition will occur at higher temperatures. The comparison of figure 4.10 with the corresponding contour plots in figure 4.3 also shows that the minima of the fcc-like structure stabilize with increasing temperature. Furthermore, calculations at higher temperatures were performed but did not yield any additional information. Of course also for these two systems the temperature evolution of all the properties, which are presented above for Fe_3Ni, has been performed.

However, the results for $Fe_{71}Ni_{29}$ are very similar to those of Fe_3Ni except for a shift of the transition temperature. Similarly, the calculated properties of $Fe_{69}Ni_{31}$ strongly resemble those of $Fe_{65}Ni_{35}$, which is discussed in more detail below in the present chapter.

(a)

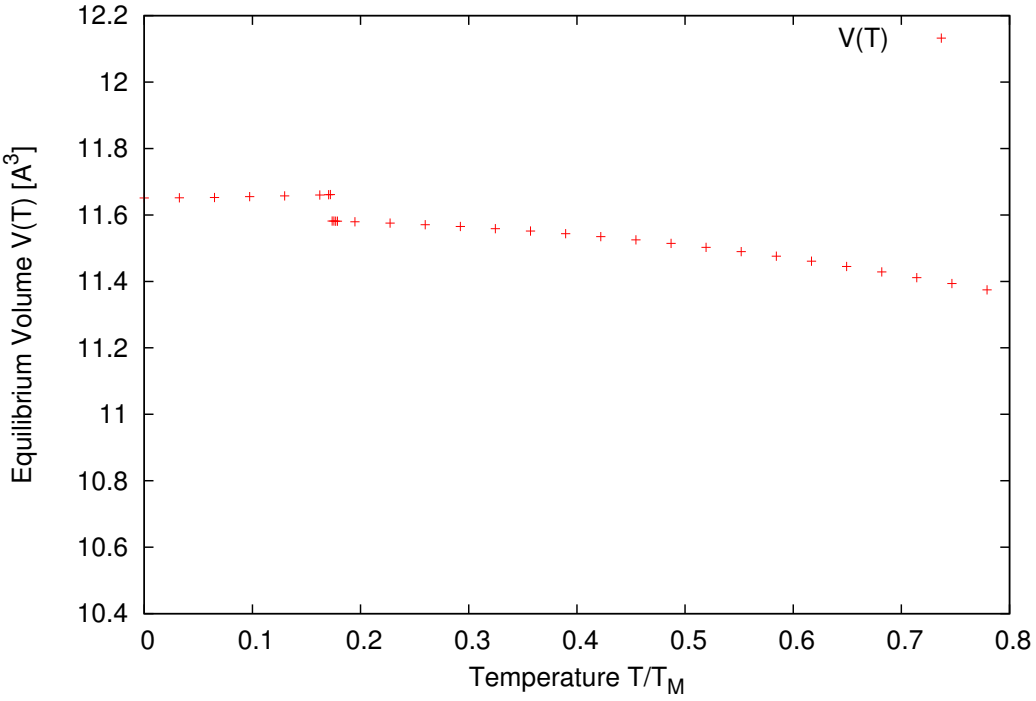

(b)

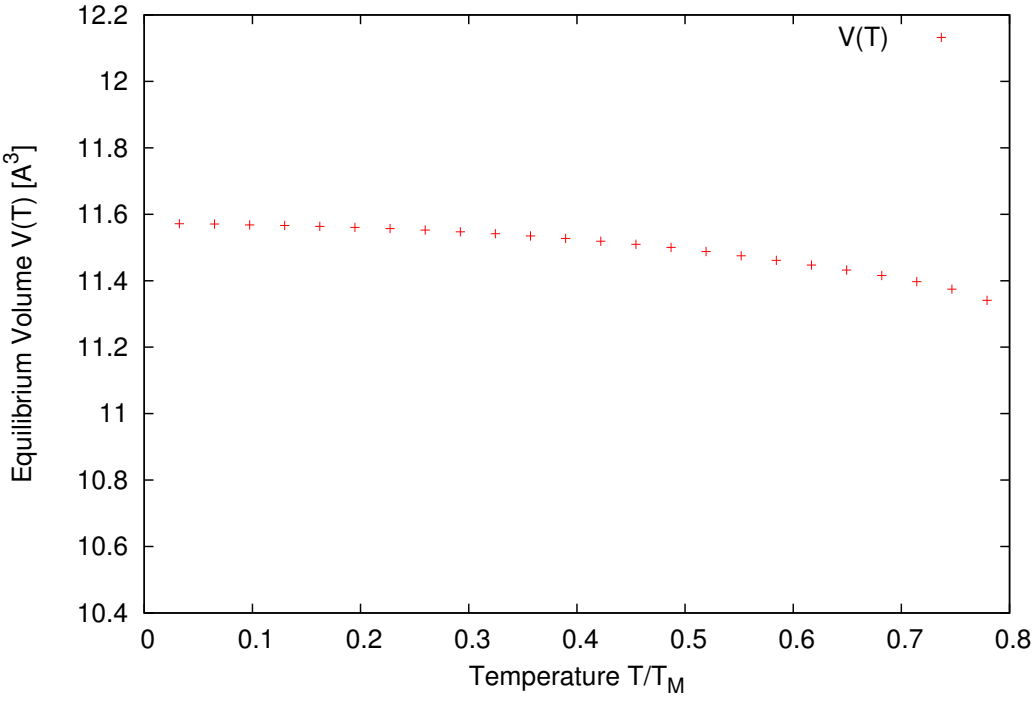

Figure 4.9: Temperature dependence of the volume for $Fe_{71}Ni_{29}$ (a) and $Fe_{69}Ni_{31}$(b). $Fe_{71}Ni_{29}$ shows a structural phase transition. Both exhibit negative thermal expansion in the fcc-like phase.

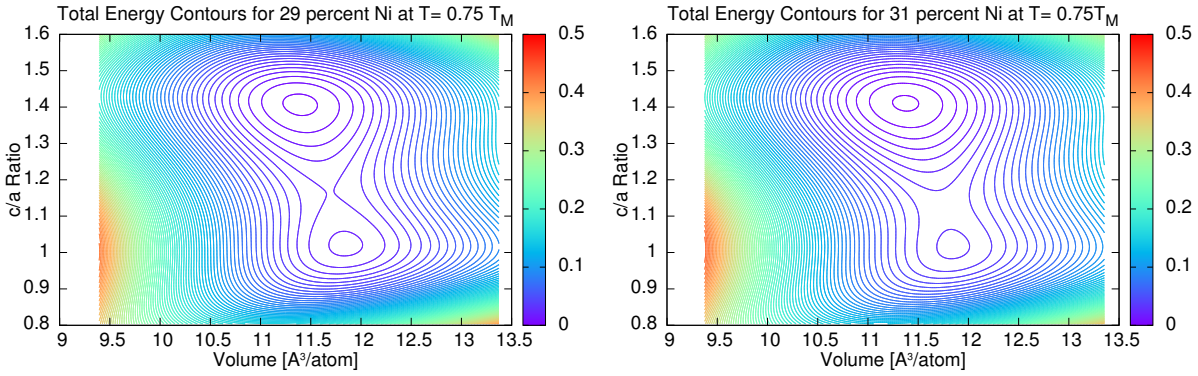

Figure 4.10: Total energy surfaces at $T = 0.75 \cdot T_{\mathrm{M}}$ for $Fe_{71}Ni_{29}$ (left) and $Fe_{69}Ni_{31}$(right). The minimum at the fcc-like structure stabilizes at high temperatures for both compositions.

Hence no further data on these two systems is presented.

An important result of this comparison is that the finite temperature modelling does not always yield a phase transition from the ground state minimum to the excited state but in the present work only the transition, which is also observed experimentally, occurs. If the initial ground state remains stable at high temperatures, the formalism even causes a stronger stabilization.

In the finite temperature modelling of $Fe_{65}Ni_{35}$ problems occurred concerning the stability of the minimization of the equations of state combined with the defining equations of the fluctuations. At $T > 0.5 \cdot T_{\mathrm{M}}$, no minimum fulfilling the criteria mentioned in section 4.3.1 could be found. Since the fluctuations increased linearly up to this value, the self-consistent solution leading to the fluctuation amplitudes was replaced with a linear approximation, as it is suggested in [33]. The defining points of the linear approximation are $T = 0$ K without any fluctuations and the fluctuations in Fe_3Ni at $T \approx 1.6 \cdot T_{\mathrm{M}}$.

At $T = 0$ K, the ground state of $Fe_{65}Ni_{35}$ is near the fcc-like structure. As for Fe_5Ni_3 (see section 3.2), the exact position of the minimum is at $c/a \approx 1.44$. Figure 4.11 illustrates that with increasing temperature, the minimum shifts towards the exact c/a-ratio of the fcc-like structure.

The temperature dependence of the volume shows that also at a Ni-content of 35 %, the fcc-like structure has a negative thermal expansion coefficient, which is depicted in figure 4.12. The behaviour of $\alpha(T)$ is unexpected, since the theories of the Invar effect presented in section 2.2.1 explain the almost vanishing thermal expansion coefficient as

(a)

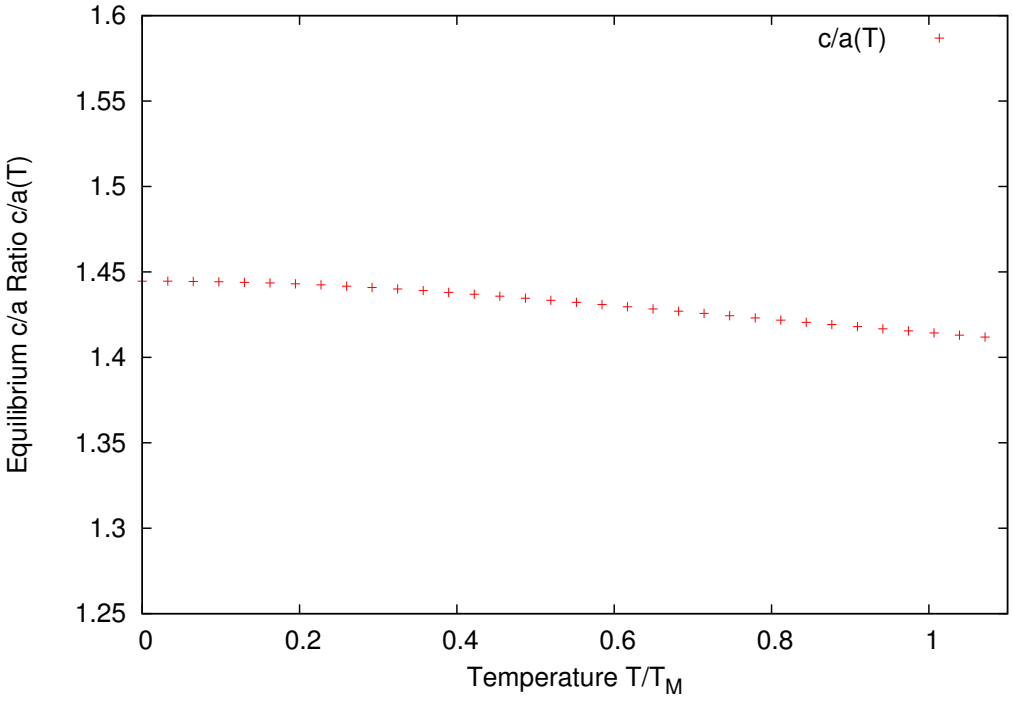

(b)

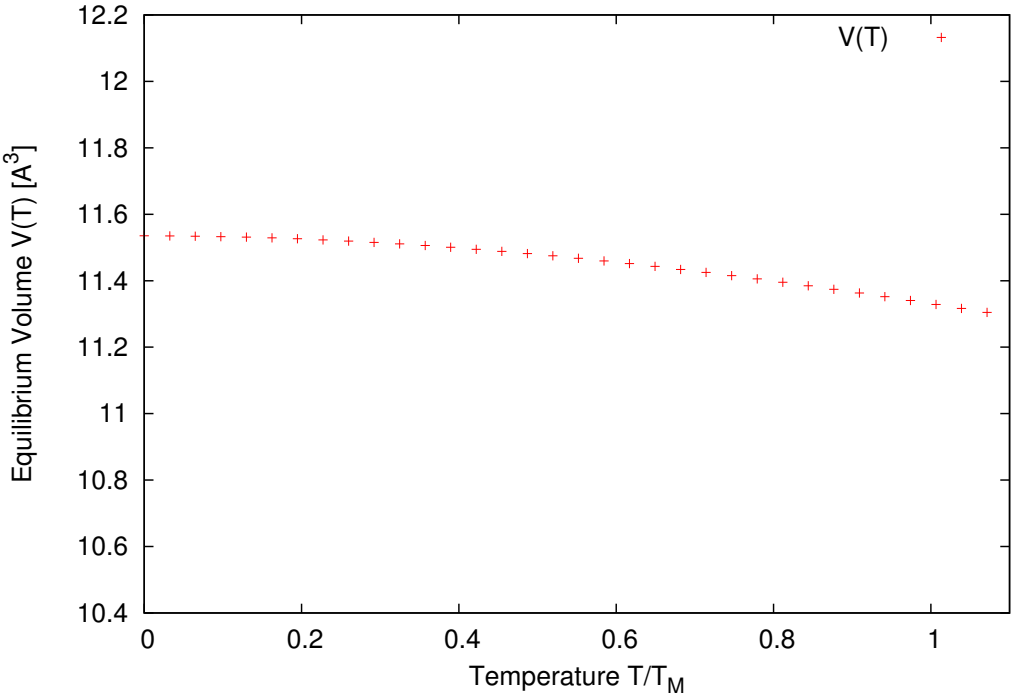

Figure 4.11: Temperature dependence of the c/a-ratio (a) and the volume (b) of $Fe_{65}Ni_{35}$. At higher temperatures the c/a-ratio shifts towards the exact fcc-like structure. The volume shows a small negative thermal expansion.

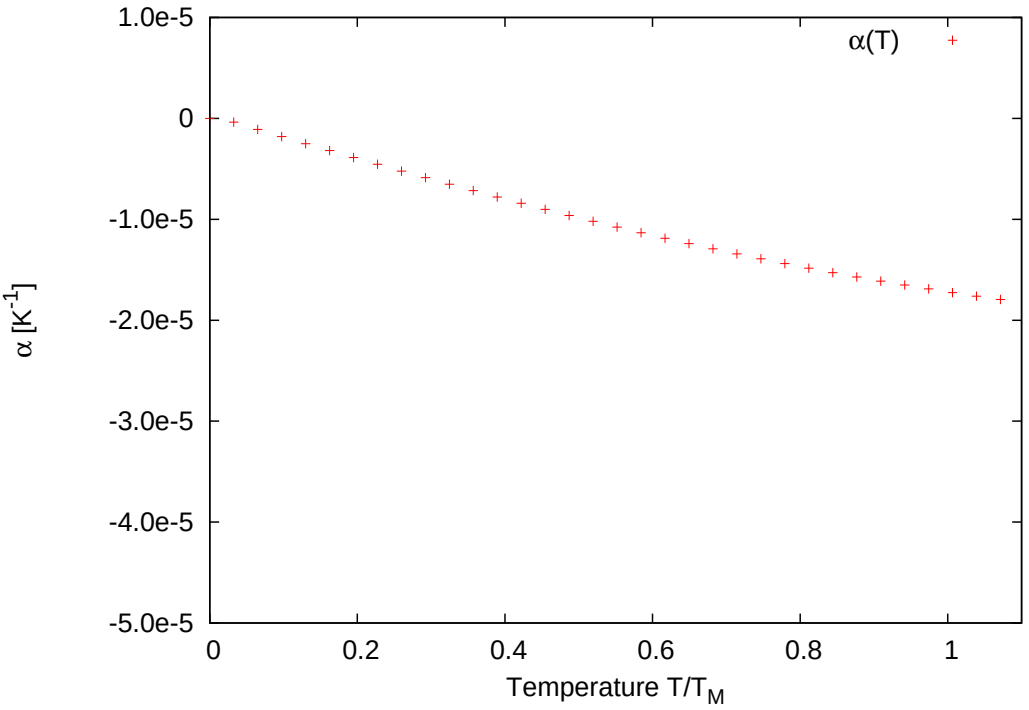

Figure 4.12: Temperature dependence of the thermal expansion coefficient α showing that it is negative and considerably smaller than in Fe_3Ni.

the combination of a positive contribution of structural effects and a contraction caused by magnetic effects. Again, the negative thermal expansion is a consequence of the shape of the energy surface. In Fe_5Ni_3, the surroundings of the minimum at constant c/a-ratio are nearly symmetric as a function of the volume. However, the energy increases slightly slower towards larger volumes. Since the surroundings of the minimum of the fcc-like structure of Fe_3Ni strongly favour negative thermal expansion, the minimum of the interpolated energy surface of $Fe_{65}Ni_{35}$ shifts towards smaller volumes in the finite temperature calculations.

Furthermore, the nearly symmetric form of the energy minimum of the fcc-like structure of Fe_5Ni_3 causes the finite temperature results to be very sensitive to the quality of the fit near the minimum. First, the assumption was made that the negative thermal expansion resulted from insufficient accuracy of the fit. However, this assumption was discarded after a very good fit in the critical area achieved by including additional data and decreasing the fit range still led to negative thermal expansion of $Fe_{65}Ni_{35}$. Thus it is clear that the results depicted in 4.12 are qualitatively correct but quantitatively depend the accuracy of the fit near the minimum of the fcc-like structure.

(a)

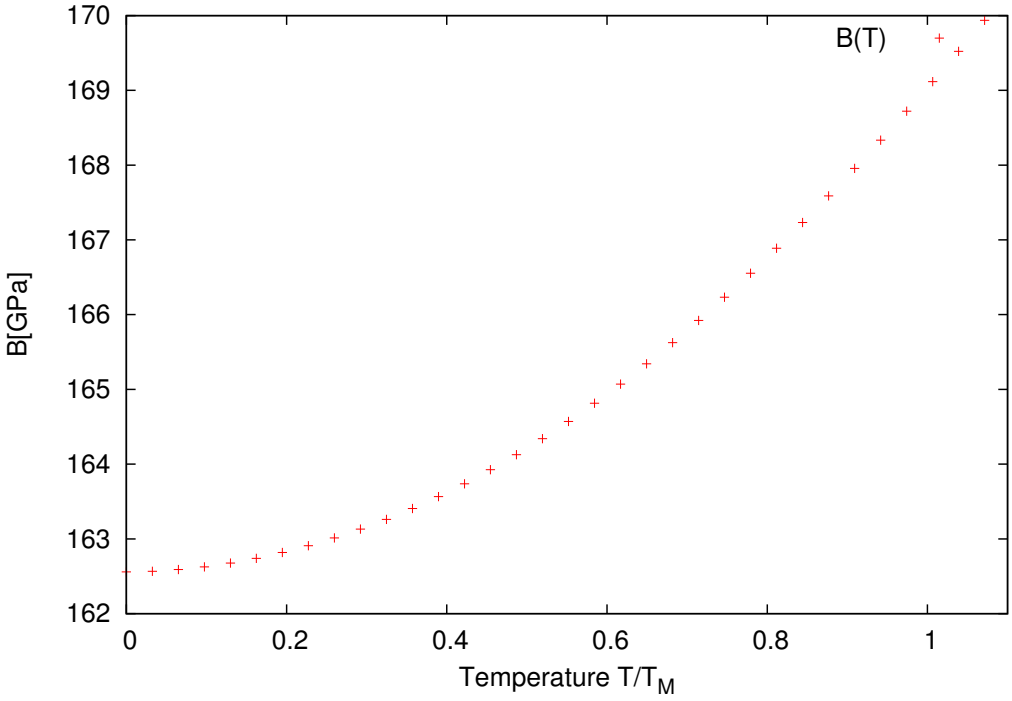

(b)

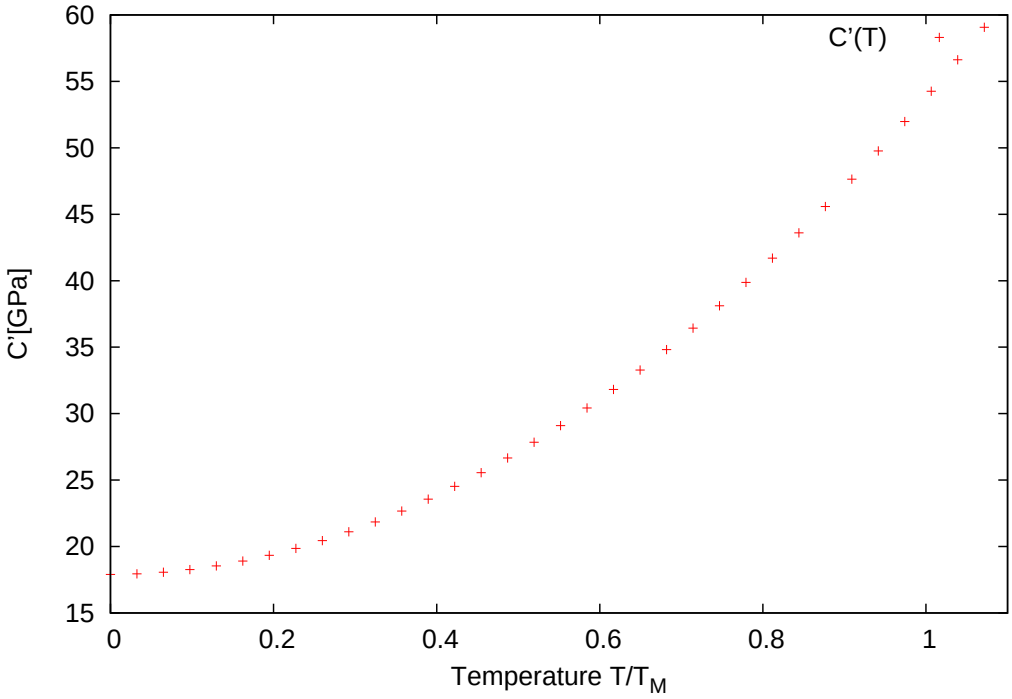

Figure 4.13: Temperature dependence of the bulk modulus B (a) and the elastic constant C' (b) of $Fe_{65}Ni_{35}$. The increase of both elastic constants shows the stabilization of the fcc-like phase against fluctuations of the volume (B) and of the c/a-ratio (C').

Since $C_{\mathrm{Ni}} = 35$ % is near the composition of the model system Fe_5Ni_3, the linear interpolation between the model systems is assumed to be a good approximation; hence a different type of interpolation is not expected to change the results significantly.
Figure 4.13 illustrates the thermal evolution of the bulk modulus B and the elastic constant C'. Both properties increase with temperature, showing the stabilization of the minimum. Since C' and B are proportional to the second derivative of the energy with respect to the c/a-ratio (C') and the volume (B), a stabler minimum with a steeper energy surface leads to larger values of B and C'. The temperature evolution of C' is very similar for all systems considered in the present work. At low temperatures small tetragonal deformations at constant volume cost significantly less energy than at higher temperatures. With increasing temperature, volume fluctuations cause the two minima in the energy surface to drift apart, leading to an increase of C'.
However, in $Fe_{65}Ni_{35}$ the bulk modulus increases by approximately five percent from $T = 0$ K to $T = T_{\mathrm{M}}$. This increase is not observed in Fe_3Ni, where the bulk modulus decreases up to the transition temperature and remains approximately constant in the fcc-like structure.

5 Summary and Conclusion

In the present work the ground state properties and the finite temperature evolution of the Invar model systems Fe_3Ni and Fe_5Ni_3 have been calculated, focussing on structural effects such as the martensitic transformation.

In order to determine whether magnetism has an important influence on the structure of the systems, static ab-initio calculations have been performed for magnetic and non-magnetic systems at various volumes and tetragonal deformations. The results show that the ground state of both systems is ferromagnetic but the crystal structure for the energy minimum is different. The present study thus goes beyond earlier investigations where the Fe_3Ni structure was used as a model system for Invar and has been forced into the fcc structure [25]. The energy minimum of Fe_3Ni is given by the bcc-like structure whereas for Fe_5Ni_3 an fcc-like structure is more favourable. However, in the non-magnetic case the ground state structure of both systems is fcc-like. It is important to notice that the onset of magnetism stabilizes the bcc structure in Fe_3Ni. This behaviour resembles pure Fe, which also shows a magnetic bcc ground state, while the non-magnetic phase would be fcc-like. Still, for all configurations the bcc-like structure and the fcc-like structure both correspond to a minimum in the energy.

For the non-magnetic state the energy barrier of the martensitic transformation (bcc-like to fcc-like or vice versa) is approximately one order of magnitude higher than for the magnetic case. This means that the formation of magnetic order is intimately entangled with the structural phase transition. Furthermore, the magnetic moment of the ground state is not invariant under changes of the volume and the c/a-ratio. Thus for a complete description of Fe-Ni Invar alloys it is indispensable to take the magnetic properties into account.

In relaxations of the ionic system, the exact ground state configurations have been determined and in a calculation using a supercell of Fe_3Ni stoichiometry and mixed structure (bcc-like and fcc-like), the formation of a tweed-like structure favouring the bcc-like phase has been observed.

In order to investigate the importance of purely structural effects in the thermal evolution of Fe-Ni Invar alloys, temperature has been introduced to the system, represented by an analytic expression of the energy as a function of the volume and the c/a-ratio. The temperature dependence is given in the form of classical fluctuations of the volume and the c/a-ratio, neglecting the changes of the magnetic moment. The analytic expressions of the energy of the model systems allow an interpolation to compositions between Fe_3Ni and Fe_5Ni_3. It is observed that the martensitic transition occurs up to a Ni-content of approximately 30 %.

For all the Fe-Ni alloys considered in the present work, the temperature dependence of the elastic constant C', the bulk modulus and the thermal expansion coefficient have been calculated. C' shows a strong increase with temperature in all systems, whereas for increasing temperature the bulk modulus decreases in the bcc-like structure and increases in the fcc-like structure. However, a complete characterization of a material is not possible with two elastic constants only; at least the shear modulus would have to be included in order to give an overview of the system's elastic behaviour.

While the thermal expansion coefficient of systems in the bcc-like structure is positive and increases approximately linearly with the temperature, in the fcc-like structure an interesting effect occurs: Owing to the shape of the energy surface $E(c/a, V)$ of Fe_3Ni the thermal expansion coefficient is negative for the majority of compositions considered in this purely structural calculation.

These results indicate that structural effects contribute an important part to the Invar anomaly and could be necessary to explain Invar behaviour completely. However, according to the results of the static ab-initio calculations ferromagnetism is an essential property of the system and therefore every theory of Invar alloys has to consider the contributions of magnetic effects.

List of Figures

Bibliography

[1] C.E. Guillaume, *Recherches sur les aciers au nickel*, C.R. Acad. Sci. **125** (1897), 235–238.

[2] P. Hohenberg and W. Kohn, *Inhomogeneous Electron Gas*, Phys. Rev. **136** (1964), B864–B871.

[3] W. Kohn and L.J. Sham, *Self-Consistent Equations Including Exchange and Correlation Effects*, Phys. Rev. **140** (1965), A1133–A1138.

[4] P.E. Blöchl, *Projector augmented-wave method*, Phys. Rev. B **50** (1994), 17953.

[5] J.P. Perdew, K. Burke, and M. Ernzerhof, *Generalized Gradient Approximation Made Simple*, Phys. Rev. Lett. **77** (1996), 3865.

[6] J.P Perdew, K. Burke, and M. Ernzerhof, *Erratum: Generalized Gradient Approximation Made Simple*, Phys. Rev. Lett. **78** (1997), 1396.

[7] G. Kresse and J. Hafner, *Ab initio molecular dynamics for liquid metals*, Phys. Rev. B **47** (1993), 558.

[8] G. Kresse and J. Furthmüller, *Efficiency of ab-initio total energy calculations for metals and semiconductors using a plane-wave basis set*, Comput. Mat. Sci. **6** (1996), 15.

[9] G. Kresse and J. Hafner, *Ab initio molecular-dynamics simulation of the liquid-metal-amorphous-semiconductor transition in germanium*, Phys. Rev. B **49** (1994), 14251.

[10] G. Kresse and J. Furthmüller, *Efficient iterative schemes for ab initio total-energy calculations using a plane-wave basis set*, Phys. Rev. B **54** (1996), 11169.

[11] N.W. Ashcroft and N.D. Mermin, *Solid State Physics*, Saunders College, 1976.

[12] M.P. Marder, *Condensed matter physics*, Wiley-Interscience, John Wiley, 2000.

[13] M. Shiga, *Invar Alloys*, Wiley-VCH Verlag GmbH & Co. KGaA, 2006.

[14] E.F. Wasserman, *Chapter 3: Invar: Moment-volume instabilities in transition metals and alloys*, Handbook of Ferromagnetic Materials, vol. 5, Elsevier, 1990, pp. 237 – 322.

[15] P. Mohn, *Magnetism in the Solid State: An Introduction*, Springer Series in Solid-State Sciences, Springer, 2005.

[16] Edmund C. Stoner, *Collective Electron Ferromagnetism*, Proceedings of the Royal Society of London. Series A. Mathematical and Physical Sciences **165** (1938), no. 922, 372–414.

[17] E. I. Kondorsky and V. L. Sedov, *Antiferromagnetism of Iron in Face-Centered Crystalline Lattice and the Causes of Anomalies in Invar Physical Properties*, J. Appl. Phys. **31** (1960), no. 5, S331–S335.

[18] Takeo Jo, *Electronic Structure of Ni-Mn and Ni-Fe Alloys*, J. Phys. Soc. Japan **40** (1976), no. 3, 715–722.

[19] R.J. Weiss, *The Origin of the 'Invar' Effect*, Proceedings of the Physical Society **82** (1963), no. 2, 281.

[20] V.L. Moruzzi, *High-spin and low-spin states in Invar and related alloys*, Phys. Rev. B **41** (1990), no. 10, 6939.

[21] H. Hasegawa, *A theory of magneto-volume effects of itinerant-electron magnets. I. Spontaneous volume magnetostriction*, J. Phys. C: Solid State Physics **14** (1981), no. 20, 2793.

[22] Y. Kakehashi, *Finite temperature theory of local environment effects in Fe-Ni alloys*, Phys. Rev. B **38** (1988), no. 1, 474.

[23] D. Wagner, *The fixed-spin-moment method and fluctuations*, J. Phys.: Condens. Matter **1** (1989), 4635–4642.

[24] P. Mohn, K. Schwarz, and D. Wagner, *Magneto-volume effects in Fe-Ni Invar: A first principles theory*, Physica B **161** (1989), 153–156.

[25] P. Mohn, K. Schwarz, and D. Wagner, *Magnetoelastic anomalies in Fe-Ni Invar alloys*, Phys. Rev. B **43** (1991), 3318–3324.

[26] B.L. Gyorffy, A.J. Pindor, J. Staunton, G.M. Stocks, and H. Winter, *A first-principles theory of ferromagnetic phase transitions in metals*, J. Phys. F: Metal Physics **15** (1985), 1337.

[27] M. van Schilfgaarde, I.A. Abrikosov, and B. Johansson, *Origin of the Invar effect in iron-nickel alloys*, Nature **400** (1999), 46.

[28] N. Cowlam and A.R. Wildes, *A search for non-collinear ferromagnetism in INVAR*, J. Phys.: Condens. Matter **15** (2003), 521.

[29] P. Entel, E. Hoffmann, P. Mohn, K. Schwarz, and V.L. Moruzzi, *First-principles calculations of the instability leading to the Invar effect*, Phys. Rev. B **47** (1993), no. 14, 8706.

[30] S. Khmelevskyi and P. Mohn, *Magnetostriction in Fe-based alloys and the origin of the Invar anomaly*, Phys. Rev. B **69** (2004), 140404.

[31] L.D. Landau and E.M. Lifschitz, *Lehrbuch der Theoretischen Physik: Statistische Physik Teil 1*, Wissenschaftlicher Verlag Harri Deutsch GmbH, 2008.

[32] K.K. Murata and S. Doniach, *Theory of magnetic fluctuations in itinerant ferromagnets*, Phys. Rev. Lett. **29** (1972), no. 5, 285.

[33] P. Mohn, K. Schwarz, and P. Blaha, *The fcc-bcc structural transition: II. A mean field model for finite-temperature effects*, J. Phys.: Condens. Matter **8** (1996), 817.

[34] R. Peierls, *On a Minimum Property of the Free Energy*, Phys. Rev. **54** (1938), 918–919.

[35] R. P. Feynman, *Slow Electrons in a Polar Crystal*, Phys. Rev. **97** (1955), 660–665.

[36] V.L. Sliwko, P. Mohn, K. Schwarz, and P. Blaha, *The fcc-bcc structural transition: I. A band theoretical study for Li, K, Rb, Ca, Sr, and the transition metals Ti and V*, J. Phys.: Condens. Matter **8** (1996), 799.

[37] K. Bhattacharya, S. Conti, G. Zanzotto, and J. Zimmer, *Crystal symmetry and the reversibility of martensitic transformations*, Nature **428** (2004), 55.

[38] E.C. Bain, *The Nature of Martensite*, Trans AIME **70** (1924), 25–35.

[39] M. E. Gruner, W. A. Adeagbo, A. T. Zayak, A. Hucht, and P. Entel, *Lattice dynamics and structural stability of ordered Fe_3Ni , Fe_3Pd and Fe_3Pt alloys using density functional theory*, Phys. Rev. B **81** (2010), no. 6, 064109.

[40] S. Kartha, T. Castan, J.A. Krumhansl, and J.P. Sethna, *Spin-Glass Nature of Tweed Precursors in Martensitic Transformations*, Phys. Rev. Lett. **67** (1991), no. 25, 3630.

[41] D. Frenkel, *Entropy-driven phase transitions*, Physica A **263** (1999), 26.

Acknowledgements

At this point I would like to express my gratitude to Prof. Peter Mohn for the interesting topic and his kind support throughout my whole diploma project. He always provided clear explanations and helpful answers to physical questions and good advice on administrative issues. I also want to thank Prof. Josef Redinger for his readiness to help with all computational issues.
Furthermore, I am very grateful to all my colleagues in the CMS group who created a very nice working atmosphere and were always ready to help with computational problems and physical questions, especially to Christoph Gruber, who always offered helpful advice and proofread the present diploma thesis. I appreciate the great time I had working with all of them and the entertaining lunch breaks and discussions.

I would like to thank my parents for their encouragement and for supporting me throughout my studies.

I am grateful to my girlfriend Christina for giving me inspiration, for supporting my ways, and for going through life by my side.

Last but not least I want to thank my friends for many inspiring discussions as well as for distracting me from work on the right occasions.